

Accepted Article

Generation of submesoscale frontal eddies in the Agulhas Current

P. Tedesco^{1*}, J. Gula¹, C. Ménesguen¹, P. Penven¹ and M. Krug^{2,3,4}

¹Univ. Brest, CNRS, IRD, Ifremer, Laboratoire d'Océanographie Physique et Spatiale (LOPS), IUEM,

29280, Brest, France.

²Council for Scientific and Industrial Research, Natural Resources and the Environment, Cape Town,
South Africa

³Department of Oceanography, Ma-re Institute, University of Cape Town, South Africa

⁴Nansen-Tutu Centre for Marine Environmental Research, Department of Oceanography, University of
Cape Town, South Africa

Key Points:

- Submesoscale frontal eddies are generated due to barotropic instability in the Agulhas Current
- The background strain provides favorable conditions for instability generation
- A new regime of variability is highlighted in addition to the two modes described by Paldor & Lutjeharms (2009)

*Pauline Tedesco, LOPS, Technopôle Brest-Iroise, Rue Dumont d'Urville, 29280 Plouzané, France
This article has been accepted for publication and undergone full peer review but has not been
through the copyediting, typesetting, pagination and proofreading process which may lead to
differences between this version and the Version of Record. Please cite this article as doi:
10.1029/2019JC015229

Abstract

This study addresses the dynamics of the Agulhas inshore front in the submesoscale range upstream of 26°E. Submesoscale frontal eddies are observed in the vicinity of Port Elizabeth (26°E) from satellite images and in observations collected from under-water gliders. Using a submesoscale-resolving numerical model ($dx \sim 0.75$ km) we are able to simulate similar submesoscale eddies. Barotropic instability is confirmed as the generation mechanism by a 1D linear stability analysis and an eddy kinetic energy budget. Kinetic energy is transferred from the mean flow to the eddies through the mean horizontal shear, which is a signature of barotropic instability. When the Agulhas Current is in a non-meandering state, submesoscale eddy generation is a recurrent process which locally drives the front's variability. Along the front, the spatial variability of barotropic instability is shaped by the background strain. A large strain aligned with the frontal axis intensifies the frontal shear upstream of 28°E while a weakening of the strain allows for barotropic instability to be triggered downstream. Although an intermittent process, the barotropic instability shows a dominant period of variability comparable with the variability of the Agulhas Current and Undercurrent.

34 1 Introduction

35 The Agulhas Current is the most intense western boundary current of the South Hemisphere with a mean transport of ~ 80 Sv (Beal et al., 2015). It flows poleward along the
 36 South African coastline between 32° E and 19° E (Lutjeharms, 2006) and forms part of the
 37 South Indian Ocean subtropical gyre (Figure 1). The Agulhas Current finds its origin in the
 38 Mozambique Channel and from south east Madagascar. Between about $19\text{--}20^{\circ}$ E, the Agulhas
 39 Current retroflects and flows eastward back into the south Indian Ocean as the Agulhas
 40 Return Current. Large anticyclones, named Agulhas Rings, which are shed at the Agulhas
 41 Retroflection transport warm and salty waters into the South Atlantic Ocean (Lutjeharms
 42 & Gordon, 1987). This heat and salt flux, named the Agulhas leakage, is thought to be
 43 a key component of the upper branch of the global overturning circulation (Weijer et al.,
 44 2002; Peeters et al., 2004; Beal et al., 2011).

45 The Agulhas Current is described as spatially “bi-modal” (Paldor & Lutjeharms, 2009;
 46 Lutjeharms, 2006) with a stable branch upstream of Port Elizabeth (26° E) and an unstable
 47 branch downstream.

48 Upstream of Port Elizabeth (26° E), the jet is narrow and flows close to a steep and
 49 straight topography. The Agulhas Current in this region is occasionally disturbed by the
 50 passage of Natal Pulses (Figure 1), solitary meanders with diameters of 50-200 km develop-
 51 ing near the Natal Bight ($\sim 31^{\circ}$ E, Figure 1) 4-5 times a year and traveling downstream
 52 (Lutjeharms, 2006; Schouten et al., 2002). Due to dissipation and/or merging processes,
 53 only a fraction of Natal Pulses (around 1.7 per year) reaches the eastern margin of the
 54 Agulhas Bank ($\sim 24^{\circ}$ E, Figure 1) (Rouault & Penven, 2011; Krug & Tournadre, 2012; Krug
 55 et al., 2014).

56 Downstream of Port Elizabeth (26° E), the current becomes increasingly unstable. In
 57 addition to Natal Pulses, frontal eddies (Schumann & Van Heerden, 1988), also called shear-
 58 edge eddies (Lutjeharms et al., 1989), with a diameter of 50-100 km, develop along the
 59 eastern margin of the Agulhas Bank (Figure 1). Further downstream, cyclonic eddies are
 60 generated from the detachment of the Agulhas Current at the tip of the Agulhas Bank
 61 (Penven et al., 2001). All these meanders and eddies are associated with features such
 62 as filaments and plumes which can intrude onto the continental shelf (Lutjeharms, 2006;
 63 Krug et al., 2014). The Agulhas retroflection ($20\text{--}19^{\circ}$ E, Figure 1) has a high level of eddy
 64 variability due to the spawning of Agulhas Rings (Lutjeharms & Gordon, 1987).

65 The first baroclinic Rossby radius of deformation (Rd) is $O(20\text{--}40)$ km in the region
 66 (Chelton et al., 1998). As the features described above are typically larger than Rd Lutje-
 67 harms (2006); Paldor & Lutjeharms (2009) historical descriptions of the Agulhas Current
 68 dynamics accounts for the mesoscale range. However, the Shelf Agulhas Glider Experiment
 69 (SAGE) (Krug et al., 2017) provides recent observations of submesoscale instabilities (L
 70 $< Rd$) in the region. In April 2015, two Seagliders sampled submesoscale frontal cyclonic
 71 eddies, with diameters ~ 15 km, offshore Port Elizabeth (Figure 2a). Features similar to
 72 the SAGE’s eddies are regularly visible on maps of Sea Surface Temperature (SST). Figure
 73 2b shows submesoscale meanders along a portion of the cyclonic inshore front ($28.5\text{--}26^{\circ}$ E),
 74 just upstream of Port Elizabeth.

75 Observations of these frontal submesoscale eddies give a new insight on the historical
 76 description of the Agulhas Current dynamics (Lutjeharms, 2006; Paldor & Lutjeharms,
 77 2009). They show features at scales smaller than the previously documented at a location
 78 where the current was reported "stable". The investigation of these submesoscale features
 79 should give a more comprehensive understanding of the Agulhas Current frontal dynamics.
 80 As a consequence of, developing at the Agulhas inshore front, these submesoscale eddies
 81 can influence the shelf dynamics and variability. Plumes, filaments and eddy shedding
 82 affect the shelf by driving horizontal water masses transport (Lutjeharms, 2006; Krug et
 83 al., 2014) and so might do the frontal submesoscale eddies. In addition, the ageostrophic

85 components of the submesoscale frontal flow lead to large vertical velocities and enhanced
 86 vertical exchanges, which can impact biogeochemistry and the primary production of the
 87 upper ocean (Mahadevan, 2014).

88 Similar examples of submesoscale frontal cyclonic eddies are reported for two other
 89 western boundary currents. In the Gulf Stream, eddies with diameters of 10-15 km were
 90 observed on satellite SST images and modeled using a submesoscale-resolving simulation
 91 (Gula et al., 2015b). In the Eastern Australian Current, eddies with diameters of 10 km
 92 were observed with coastal HF radars and satellites (Schaeffer et al., 2017). In addition,
 93 frontal submesoscale eddies may also be of interest for the ocean energy budget as they can
 94 trigger an energy route from the large-scale geostrophic circulation toward smaller scales
 95 (Ferrari & Wunsch, 2010).

96 In this study, we address the dynamics of the Agulhas inshore front around Port Eliz-
 97 abeth (26° E) using a submesoscale-resolving numerical model. We aim to characterize the
 98 frontal submesoscale eddy generation mechanism, its spatial and time variability and the
 99 factors involved in their triggering. In section 2, we present the numerical simulations. In
 100 section 3, we compare the modeled mean dynamics of the Agulhas Current with *in situ* and
 101 satellite observations. In section 4, we investigate the generation mechanism of the subme-
 102 sesoscale eddies in the model. Finally, in section 5 we discuss the spatial and time variability
 103 of the submesoscale eddy generation mechanism.

104 2 Simulation setup

105 The realistic simulations are run with the CROCO (Coastal and Regional Ocean COM-
 106 munity model) model (Debreu et al., 2012), which is based on ROMS (Shchepetkin &
 107 McWilliams, 2005). This model solves the hydrostatic primitive equations for the momen-
 108 tum and the state variables and uses topographic following vertical coordinates.

109 To set up a submesoscale eddy-resolving simulation, we use a nesting approach. Four
 110 nests with respective horizontal resolutions of $dx \sim 22.5, 7.5, 2.5$ and 0.75 km are embedded
 111 (Figure 3). The highest-resolution grid ($dx \sim 0.75$ km) has a sufficient effective horizontal
 112 resolution (Soufflet et al., 2016) to solve the submesoscale range ($< O(30)$ km) in the Agulhas
 113 region.

114 The three first nests ($dx \sim 22, 7.5$ and 2.5 km) are set up with the same nesting pro-
 115 cedure, forcings and vertical grid. The nesting procedure is a two-way online nesting based
 116 on AGRIF (Debreu et al., 2012). At each time step each "child" grid is forced by its "par-
 117 ent" grid and feedbacks from the "child" grids (finer scales) to larger grids (larger scales) are
 118 taken into account. The GLORYS oceanic reanalysis (Ferry et al., 2012) provides the lateral
 119 boundary conditions for the largest grid ($dx \sim 22$ km). The surface forcings are provided by
 120 a bulk formulation (Fairall et al., 1996) using the daily ERA-ECMWF's reanalysis (Dee et
 121 al., 2011). Relative winds are preferred to absolute winds due to their implications in a more
 122 realistic dissipation of mesoscale eddies in the Agulhas Current (Renault et al., 2017). The
 123 bathymetry is built from the General Bathymetric Chart of the Oceans 30-sec resolution
 124 (Gebco 2014). The topography is locally smoothed when steepness exceeds the threshold
 125 $r_{max} = 0.2$, with $r_{max} = \frac{\nabla h}{h}$ the slope parameter defined by Beckmann & Haidvogel (1993).
 126 The vertical grids are designed following the Haidvogel & Beckmann (1999) method. Pa-
 127 rameters driving the levels refinement at the surface and the bottom are respectively $\theta_s =$
 128 5 , $\theta_b = 0$. The transition depth between flat-z levels and terrain following sigma level is set
 129 to $h_{cline} = 10$ m.

130 The highest-resolution grid ($dx \sim 0.75$ km) set up differs from the three first grids on
 131 several points. The nesting procedure is an offline one-way nesting as described by Gula
 132 et al. (2015a). In this case, the parent forces the child grid without feedback from the
 133 finer toward the larger scales. The surface forcing and the bathymetry are derived from the
 134 same datasets as for parent grids. The boundary conditions are provided by the nearest

parent grid ($dx \sim 2.5$ km) at a daily rate. The vertical resolution is increased relative to the horizontal resolution with 100 vertical levels. They are distributed following Lemarié et al. (2012) method with parameters $\theta_s = 6$, $\theta_b = 4$ and $h_{cline} = 300$ m.

The horizontal advection of momentum is discretized using a 3rd order upstream biased numerical scheme and horizontal advection of tracers is discretized using a split and rotated 3rd order upstream-biased numerical scheme (Marchesiello et al., 2009). The later scheme reduces spurious diapycnal mixing. On the vertical, the momentum advection scheme is semi-implicit, with an adjustment between explicit and implicit formulation according to the model stability.

A K-profile parameterization (KPP) (Large & Yeager, 2004) parameterizes the vertical mixing of tracers and momentum. The adjusted KPP by Durski et al. (2004) is used for the bottom boundary layer. Both parameterizations take into account the Lemarié et al. (2012)'s modification of the Richardson number criterion with the critical value ($Ri_{cr} = 0.15$). The bottom viscous stress has a quadratic form.

The parent grid ($dx \sim 22.5$ km has 450 x 258 x 60 points) covers most of the South Equatorial Indian Ocean and a part of the Atlantic Ocean. The first child grid ($dx \sim 7.5$ km), with 578 x 542 x 60 points, encompasses the African continent from the Equator to the Antarctic Circumpolar Current. It includes the Mozambique Channel, where large anticyclones are generated (Halo et al., 2014) and related to Natal Pulses development in the Agulhas Current (Eliot & Beal, 2015). Both nests are spun-up from their initial state for 3 years. The third child grid ($dx \sim 2.5$ km), with 674 x 578 x 60 points, encompasses the Agulhas Current from upstream the Natal Bight ($\sim 31^{\circ}$ E) to the Agulhas retroflection region ($\sim 19\text{--}20^{\circ}$ E). This simulation is spun up for a year and run from 1993 to 2014. The highest-resolution grid ($dx \sim 0.75$ km has 1352 x 652 x 100 points) is centered on the SAGE area (Port Elizabeth, 26 °E) and resolves more precisely the submesoscale dynamics of the current and their potential interactions with the topography. This grid is run from 01/09/1995 to 31/03/1997. This period is centered on the year 1996, during which no upstream Agulhas retroflection is observed or simulated.

3 Observed and modeled Agulhas dynamics

In this section, we evaluate the mean Agulhas Current dynamics. First, we compare the mean modeled surface Agulhas Current to satellite data and second, we compare the vertical and the surface structures of the mean modeled Agulhas inshore front, in the vicinity of our area of interest (Port Elizabeth, 26°E) with *in situ* data.

3.1 The mean Agulhas Current: surface description

The mean Eddy Kinetic Energy (\overline{EKE}) is defined as $\overline{EKE} = 0.5(\overline{u'^2} + \overline{v'^2})$ with u and v the horizontal velocity components. The overbar denotes a time mean and the prime denotes fluctuations relative to this mean. We compare the surface \overline{EKE} from the $dx \sim 2.5$ km nest with the one derived from satellite altimetry observations of absolute dynamic topography gridded at 1/4° provided by AVISO (Figure 4). Both observed and modeled \overline{EKE} are defined from geostrophic velocity anomalies diagnosed from a 10-year long subset (1993–2003) of sea surface height anomaly.

The modeled and observed surface \overline{EKE} patterns match the spatially "bi-modal" dynamics of the Agulhas Current. Upstream of Port Elizabeth (26°E), \overline{EKE} is low ($O(0.5\text{--}2) 10^3 \text{ s}^{-2}$) and downstream it is more intense ($O > (3.5) 10^3 \text{ cm}^2 \text{ s}^{-2}$). The Agulhas retroflection region, where Agulhas Rings and Agulhas Eddies are generated, has the largest values of \overline{EKE} . The Agulhas Return Current \overline{EKE} has moderate values ($O(2\text{--}3) 10^3 \text{ cm}^2 \text{ s}^{-2}$) reflecting the two standing meanders found at the Agulhas Plateau (26°E) and at 32°E. The observed and the modeled \overline{EKE} magnitudes differ upstream of 23°E. The difference is

the largest at the Agulhas Bank eastern margin (25°E - 23°E). The model shows an intense \overline{EKE} , with values of the same order as at the Retroflection area, whereas AVISO shows a lower magnitude ($O(1.5) \cdot 10^3 \text{ cm}^2 \text{ s}^{-2}$). This area is where Natal Pulses can be trapped and grow in size (Krug et al., 2014) and where Shear-Edge eddies can develop (Lutjeharms et al., 1989) and potentially leak downstream. The amplitude difference between the two datasets can be explained by their different spatial resolutions. AVISO spatial effective resolution is $\lambda \sim 100 - 150 \text{ km}$ (Chelton et al., 2011) whereas the $\text{dx} \sim 2.5 \text{ km}$ nest has an effective resolution of about $\lambda \sim 10\text{dx} \sim 25 \text{ km}$ (Soufflet et al., 2016). Hence, scales in the range of 10 - 70 km seem to drive the Agulhas Current variability at the Agulhas Bank eastern margin. The relationship between the relaxation of the topographic constraint on the current and the development of intense perturbations (Lutjeharms, 2006; Paldor & Lutjeharms, 2009) is visible in the modeled \overline{EKE} . Areas of intense \overline{EKE} are associated with the current path (sea surface height contours in green) separating from the topography (1000 m isobath is the most inshore black contour).

3.2 The Agulhas Current upper branch (upstream of Port Elizabeth): description of the inshore front

3.2.1 Mean vertical structure of the Agulhas Current at 28.5°E : comparison with ACT data

The Agulhas Current mean vertical structure from the 1 year-long simulation of the highest-resolution nest ($\text{dx} \sim 0.75 \text{ km}$) is compared to the Agulhas Current Time-series Experiment (ACT) data (Figure 5). ACT is a 34 month-long time series (April 2010-February 2013) of current measurements undertaken from a mooring array across the Agulhas Current at 28.5°E (Beal et al., 2015).

The modeled Agulhas Current has a vertical structure close to the one observed during the ACT experiment. They both have a similar width of 200 km, defined as the distance between the 0 m s^{-1} velocity contour (Figures 5a, c), in the upper ocean. In the model, the current extends slightly further offshore than in the observations and does not intrude significantly onto the continental shelf. This results in a clear delimitation between the shelf waters and the Agulhas Current. The modeled and observed currents have a similar vertical structure, with a v-shape typically associated with surface intensified flows. The mean Agulhas Current velocities reach values larger than -1.5 m s^{-1} at the surface and the current core, defined by the -0.5 m s^{-1} contour, extends over a width of about 100 km at the surface and is 800 m deep. These similarities in the mean Agulhas structure are reflected in the net volume flux (T_{box} in Beal et al. (2015)) : $-77 \pm 5 \text{ Sv}$, for the ACT data and -79.6 Sv for the highest-resolution nest.

The modeled and observed Agulhas inshore fronts have high values of cyclonic relative vorticity which is uniform from the surface to about 500 m depth (Figures 5b and d). The modeled front is more intense with relative vorticity values up to $O(3f)$ compared to the observations of $O(0.5f)$. This magnitude difference could suggest different mean current structures. The modeled current does not spread onto the continental shelf and this results in a sharper front at the shelf break. However, the coarser horizontal resolution of the ACT data, which cannot resolve the sharp current gradients at the inshore front of the Agulhas Current, must also contribute to this difference.

The agreement between the highest-resolution nest and the ACT data also includes the Agulhas Undercurrent mean vertical structure. Below the Agulhas Current flows a weaker equatorward current : the Agulhas Undercurrent (Figures 5a and c). Both modeled and observed deep currents show a vein of weak north-easterly flow between 1500 and 3000 m over a width of 50 km. This undercurrent embraces the topography and is associated with mean velocities of about 0.03 m s^{-1} and peaking up to 0.08 m s^{-1} where it is the closest to the topography.

**233 3.2.2 Mean surface structure of the Agulhas cyclonic front at 25.75°E:
234 comparison with SAGE data**

The Agulhas Current mean surface structure, along the SAGE section (25.75°E), from the four model nests ($dx \sim 22.5, 7.5, 2.5$ and 0.75 km) are compared to glider data from SAGE (Figure 6). With the SAGE dataset, the cross-front section is computed by averaging the data in the along-front direction and over the one month-long record. The model sections are computed following the same steps for a period equivalent to the SAGE one. In the model, the one-month period is chosen in order to get similar dynamical conditions as during the SAGE experiment regardless of the dates. This one-month period corresponds to a period without mesoscale meanders, *i.e* a nonmeandering state, the 1000 m isobath marks the mean inshore front position (not shown here) and submesoscale eddies are present. Contrary to the SAGE period, no northeastward current on the shelf is present during the one-month period in the model. The origin of this feature on the shelf is unclear (Krug et al., 2017) and it is shown in the next sections that it is not a limiting factor for our study.

The highest-resolution nest ($dx \sim 0.75$ km) best fits with SAGE observations. The modeled and observed along-front velocities have close cross-front patterns and magnitude offshore of the shelf (about -1 m s $^{-1}$ at the inshore front location). The modeled vorticity shows a pattern typical of sheared flows, with a peak of $O(2f)$ at the front location, whereas the observed vorticity reaches a threshold at the front ($O(1f)$) and increases offshore. The limited number of observations collected during SAGE could explain why the modeled and observed relative vorticity cross-front profiles differ. The gliders did not go further offshore to catch the maximum magnitude of the current and hence cannot show a decrease after reaching a relative vorticity maximum.

All the modeled cross-front sections, relative to different numerical resolutions, show different patterns. This suggests that the highest-resolution nest did not converge yet. While the $dx \sim 22.5$ and 7.5 km nests have flat cross-front patterns, the $dx \sim 2.5$ and 0.75 km nests show gradients of mean along-front velocity and mean vorticity peaking at the mean Agulhas inshore front position (1000 m isobath). The lack of convergence means the highest-resolution nest could be numerical resolution-dependent. This could also explain the different relative vorticity cross-front patterns between the model and SAGE. However, in the next sections it is shown that in spite of the lack of convergence, the highest-resolution nest and SAGE captured the same frontal dynamics.

In this section, we show that the model captures the mesoscale variability of the Agulhas Current (Figure 4). Perturbations are the most energetic along the downstream branch of the current: at the Agulhas Bank, at the Retroflexion and along the Agulhas Return Current. In the vicinity of Port Elizabeth (26°E), the model shows, in good agreement with *in situ* data, that the mean Agulhas inshore front has an intense cyclonic relative vorticity ($O(> f)$) that is uniform from the surface to about 500 m depth (Figure 5). Despite the respective limitations of the model and SAGE data - the model might not have converged yet and the glider data are sampled over a limited area - the modeled mean-state is similar to the SAGE one (Figure 6). We also validated the modeled water masses at the ACT array against the CARS climatology (K.R. Ridgway & Wilkin, 2002) (not shown here).

75 4 Submesoscale eddies along the Agulhas cyclonic front

In this section, we describe the submesoscale frontal eddies in the model, we investigate barotropic instability as the generation mechanism proposed by Krug et al. (2017), and we evaluate its importance in driving the Agulhas inshore front variability.

279 4.1 Description of the submesoscale cyclonic eddies in the SAGE area

280 Submesoscale eddies (diameters of 10-20 km) develop along the Agulhas inshore front
 281 upstream of Port Elizabeth (26°E) in the highest-resolution nest (Figure 7). Several eddies
 282 develop simultaneously between 28°E and 26°E, over a portion of the front where the current
 283 flows closely to the topography, and forms a vortex street. In the model, submesoscale eddies
 284 are generated on a quasi-regular basis. They have a limited life-time ($\sim 3\text{-}4$ days). Once
 285 developed, they propagate downstream, in the opposite direction of Kelvin waves, over 300-
 286 400 km before dissipating. Along the Agulhas Bank (westward of Port Elizabeth, 26°E),
 287 the topographic constraint on the front relaxes. As a result, the submesoscale eddies can
 288 grow to diameters of 40-50 km, beyond the submesoscale range.

289 The size and location of the modeled submesoscale eddies are consistent with the sub-
 290 mesoscale eddies captured during SAGE (Krug et al., 2017) and observed on SST satellite
 291 images (Figure 2).

292 The submesoscale eddies are intensified at the surface and associated with a cold tem-
 293 perature anomaly (Figure 8). With values of $(O(5\text{-}10)f)$, the relative vorticity is the largest
 294 in the eddy cores and within the upper 25 m (Figure 8 top panel). Their core temperatures
 295 range from 15 to 19°C and at the edges it ranges from 20 to 23°C (Figure 8 bottom panel).
 296 The cold temperature anomaly is related to the cyclonic motion of the eddies which induces
 297 an upward doming of the isotherms. Water mass horizontal transfer during the process
 298 of the front destabilization can also reinforce the eddy temperature anomaly. In fact, the
 299 Agulhas front, characterized by warm water, develops cross-frontal meanders which extend
 300 onto the shelf and trap local cold water when they grow into finite amplitude and form the
 301 cyclonic eddies.

302 4.2 Barotropic instability as the generation mechanism

303 The Agulhas inshore front is barotropically unstable before the submesoscale eddy gen-
 304 eration. The submesoscale eddies develop along a current portion where the mean velocity
 305 shear is intense (Figures 5 and 6) and such flows are prone to barotropic instability. A nec-
 306 essary condition for this instability is a change of sign of $\frac{d^2\bar{U}}{dy^2}$, with y the cross-front direction
 307 and $U(y)$ the along-front velocity component. A typical velocity profile $U(y)$, selected from
 308 the highest-resolution nest below the surface (5 m) upstream of the eddy generation site
 309 (28°E) and at a time just before eddies develop (Figure 9, top panel), satisfies the instability
 310 condition.

311 Perturbations originating from the barotropically unstable velocity profile are coherent
 312 with the submesoscale eddies. A linear stability analysis is performed with the modeled
 313 velocity profile shown in Figure 9. The Boussinesq eigenvalue problem described by Mé-
 314 nesguen et al. (2012) is modified to a 1D horizontal problem. The linear stability prob-
 315 lem is solved for a typical velocity state $U(y)$ and normal modes for the perturbations
 316 $\{u(y), v(y), p(y)\} \exp^{i(my)} \exp^{\sigma t}$, with y the cross-front direction, u and v the along and
 317 cross-front velocity components, p the pressure, m the non-dimensional x-wavenumber, t
 318 the time and σ the perturbation growth rate. For this 1D configuration, the adimensional-
 319 ized Boussinesq equations for momentum are :

$$\begin{aligned} Ro[\sigma v + imUv] - u + \partial_y p - Ek\Delta'v &= 0 \\ Ro[\sigma u + \partial_y Uv - imUu] + v + imp - Ek\Delta'u &= 0 \\ \partial_y v + imu &= 0 \end{aligned} \quad (1)$$

320 with $\Delta' = \partial_{x^2}^2 - m^2$.

321 The initial velocity profile $U(y)$ corresponds to the function : $U(y) = U_0 \tanh(\frac{y}{d}) + U_1$
 322 fitted to the velocity profile from the highest-resolution nest (Figure 9, top panel), with $U_0 =$
 323 -1.09 m s^{-1} the typical velocity magnitude, $d = 830 \text{ m}$ the shear width and $U_1 = -0.32 \text{ m s}^{-1}$

a constant. For the system of equations 1, the 1D flow is governed by two non-dimensional numbers : the Rossby and the Ekman numbers. The Rossby number $Ro = \frac{U_0}{fd}$, with f the Coriolis parameter, is the ratio of inertial to rotation terms and is as large as $Ro = 16$. The Ekman number $Ek = \frac{\nu}{fd^2}$, with ν the viscosity, is the ratio of diffusion to rotation terms and is kept very small (10^{-6}) to correspond to inviscid flow.

The fastest growing modes have wavelengths of 10-13 km (Figure 9). The 1D linear stability analysis points out perturbations in the same scale range as the submesoscale eddies in the highest-resolution nest (10-20 km) and as the ones captured by SAGE and observed on the SST satellite images (~ 15 km).

The parameter d corresponds to the shear width and it is close to the numerical resolution: $dx \sim 0.75$ km. This is consistent with the possible non-convergence of the highest-resolution nest, as hinted by Figure 6 and this means that the mean velocity shear amplitude could be limited by the model viscosity. However, this is also counterbalanced by the modeled shear being of the same order of magnitude as the shear measured during SAGE (Figure 6).

This preliminary analysis, led for a specific time of submesoscale eddy generation, supports Krug et al. (2017)'s suggestion that barotropic instability is the main generation mechanism.

The eddy energy source, identified for the same episode of submesoscale eddy generation, confirms the prevalence of barotropic instability. The \overline{EKE} equation is (Gula et al., 2016b):

$$\underbrace{\frac{1}{2} \overline{\frac{\partial u_i'^2}{\partial t}}}_{\frac{\partial EKE_i}{\partial t}} + \underbrace{\frac{\partial}{\partial x_i} \left(\frac{1}{2} \overline{u_j u_i'^2} + \frac{1}{2} \overline{u_j' u_i'^2} + \frac{1}{\rho_0} \overline{u_j' p'} \right)}_{Boundary\ transport} = \underbrace{- \overline{u_j' u_i'} \frac{\partial \overline{u_i}}{\partial x_j}}_{MKE \rightarrow \overline{EKE}} + \underbrace{\overline{w' b'}}_{EPE \rightarrow \overline{EKE}} + \underbrace{\overline{V_i' u_i'}}_{Vertical\ mixing} + \underbrace{\overline{D_i' u_i'}}_{Horizontal\ diffusion} \quad (2)$$

$$\text{with } MKE \rightarrow \overline{EKE} = - \overline{u_i' u_i'} \frac{\partial \overline{u_i}}{\partial x_i} - \overline{u_i' w'} \frac{\partial \overline{u_i}}{\partial z} \text{ and } EPE \rightarrow \overline{EKE} = \overline{w' b'}$$

The Cartesian tensor notation with summation convention is used with $i = 1,2$ and $j=1,2,3$. u_i are the horizontal velocity components, $u_3=w$ is the vertical velocity, p is the pressure anomaly, $b = \frac{-g\rho}{\rho_0}$ is the buoyancy anomaly, V_i' is the vertical mixing, with $V_i' = \frac{\partial}{\partial z} \left(K_M v \left(\frac{\partial u_i'}{\partial z} \right) \right)$ and D_i' is the horizontal diffusion term in the horizontal momentum equations, computed as the difference between the third-order upwind numerical advective momentum scheme and the fourth-order centered scheme (Gula et al., 2014). The overbar denotes a time mean and the prime denotes fluctuations relative to this mean. In Equation 2, the terms from the left hand side correspond to the Eulerian time derivative and to the boundary transport of \overline{EKE} , due to pressure fluctuations and advection by the mean and fluctuating current components, whereas the terms from the right hand side correspond to the local sources and sinks. The two terms $MKE \rightarrow \overline{EKE}$ and $EPE \rightarrow \overline{EKE}$ are possible \overline{EKE} sources while vertical mixing and lateral diffusion are the main sinks. The barotropic instability signature on energy transfer is a positive $MKE \rightarrow \overline{EKE}$ transfer through its horizontal component: \overline{HRS} . It corresponds to an energy extraction from the mean horizontal shear toward the growing perturbations.

The three possible \overline{EKE} sources (\overline{HRS} , \overline{VRS} and \overline{VBF}) are averaged over a one-week period which corresponds to the full period of the submesoscale eddy generation event previously investigated (Figure 10). Along the front portion, where the submesoscale eddies

364 develop (28–26°E), \overline{HRS} is positive and has the highest magnitude whereas \overline{VRS} and \overline{VBF}
 365 are lower and mainly negative. \overline{HRS} is here the dominant energy source term for the
 366 perturbations ($MKE \rightarrow EKE$). This confirms the role of barotropic instability for the
 367 generation of submesoscale eddies along the Agulhas Current inshore front. The instability
 368 process is thus very similar to the development of barotropic instabilities in the submesoscale
 369 range described for the Gulf Stream (Gula et al., 2015b).

70 The vertical structure of the energy conversion term \overline{HRS} matches the surface-intensified
 371 structure of the submesoscale eddies (Figure 10). Indeed, along the vortex street (29.5–25°E)
 372 the energy conversion term is intensified from the surface to a depth of about 50 m.

373 In this subsection, we focus on a specific event of submesoscale eddy generation (Figures
 374 7 and 8). In the next subsection, we show that the generation of submesoscale eddies by
 375 barotropic instability is recurrent in this region and we discuss its predominance in driving
 376 the local variability of the Agulhas inshore front.

377 4.3 Barotropic instability as a locally preponderant mechanism

378 The triggering of the barotropic instability along the Agulhas inshore front is compared
 379 between the model and the SAGE data. With the one-month long glider dataset, a partial
 380 \overline{HRS} term can be computed along a cross-front section at 25.75°E (Krug et al., 2017).
 381 This partial term accounts for the cross-front derivative subterms : $-\overline{u'v'\partial_y\bar{u}} - \overline{v'v'\partial_y\bar{v}}$,
 382 the overbar denotes a monthly time average, which corresponds to the full SAGE period,
 383 and the prime denote fluctuations relative to this time mean. This partial \overline{HRS} term is
 384 positive and reaches a maximum at the Agulhas front. This result should be considered
 385 with caution since it involves several approximations on spatial and time averages and their
 386 findings might be limited by their use of a partial \overline{HRS} .

387 The modeled partial \overline{HRS} term, computed over a equivalent period to the SAGE one
 388 (presented in the subsection 3.2.2, Figure 6), is compared to the SAGE one along the SAGE
 389 section (25.75°E) (Figure 11). The modeled (blue lines) and the observed (red line) \overline{HRS}
 390 have similar patterns. They reach a maximum energy conversion rate inshore the 1000 m
 391 isobath, corresponding to the mean front location, with close magnitudes : $6 \cdot 10^{-6}$ and $1.08 \cdot 10^{-5} \text{ m}^2 \text{ s}^{-3}$ respectively. These maximum values are also in agreement with those found
 392 in the Gulf Stream ($1 \cdot 10^{-5} \text{ m}^2 \text{ s}^{-3}$) by Gula et al. (2015b). Hence, the approximations
 393 on spatial and time averages required by the SAGE data for the \overline{HRS} computation do not
 394 create a strong bias in the energy conversion term. Similarly, the presence of a northeastward
 395 current on the shelf during the SAGE experiment (Figure 6), which is absent in the model,
 396 does not create discrepancies relevant for the Agulhas inshore frontal dynamics.

397 The energy transfer $MKE \rightarrow EKE$ realized by the \overline{HRS} term is mainly attributable to
 398 the mean current lateral shear : $-\overline{u'v'\partial_y\bar{u}}$. In the model, the partial and the full versions of
 399 the \overline{HRS} term: $-\overline{u'u'\partial_x\bar{u}} - \overline{v'u'\partial_y\bar{u}}$, with \mathbf{u} the vector of the horizontal velocity components,
 400 are compared. Both terms show the same patterns with only small magnitude differences.
 401 Since the upstream Agulhas Current is a coastal jet constrained by a steep and straight
 402 topography, its frontal structure is dominated by the cross-shelf structure. Hence, Krug et
 403 al. (2017)'s estimation of the energy conversion at the Agulhas inshore front using a partial
 404 \overline{HRS} term is valid at the first order. In a configuration such as the upstream Agulhas
 405 Current, the estimation of the \overline{HRS} term using only the cross-front subterms is a workable
 406 approximation.

407 Submesoscale eddy generation by barotropic instability is a recurrent process when the
 408 Agulhas Current is not in a meandering state. The one-year long numerical simulation
 409 provides the ability to check the impact of time-averaging on the cross-front \overline{HRS} pattern.
 410 The one-month average is defined in order to fit the SAGE's conditions: non-meandering
 411 state, the mean front position along the 1000 isobath and submesoscale eddies developing.
 412 The five-month average is instead defined as the consecutive months for which the current

414 is not in a meandering state. Both time averages show similar patterns with slightly larger
 415 values for the five-month average.

416 Submesoscale eddy generation by barotropic instability is a recurrent process along the
 417 Agulhas inshore front between 28°E and 26°E. The \overline{HRS} term averaged over a five-month
 418 period (Figure 12) is very similar to the \overline{HRS} term averaged over the one-week period
 419 corresponding to the submesoscale eddy generation event of Figure 10. For both time
 420 periods, \overline{HRS} has a very similar pattern with positive values ($O(2.10^{-3}) \text{ m}^3 \text{ s}^{-3}$) all along
 421 the front. Other energy conversion terms \overline{VRS} and \overline{VBF} have lower magnitudes (about
 422 $O(0.25 \cdot 10^{-3}) \text{ m}^3 \text{ s}^{-3}$) and have respectively negative and an alternation of negative and
 423 positive patterns along the front (not shown here). In addition to being a recurrent process,
 424 the generation of submesoscale eddies is the major process driving the local dynamics and
 425 variability of the Agulhas inshore front in a non-meandering state in the vicinity of Port
 426 Elizabeth (26°E). In the model, Natal Pulses inhibited the development of submesoscale
 427 eddies, but these mesoscale meanders can still host submesoscale activity following the
 428 mechanisms described by Gula et al. (2016a) in the context of Gulf Stream frontal eddies.

429 In this section, we confirm barotropic instability as the submesoscale eddy generation
 430 mechanism. The submesoscale eddies are recurrent features which locally drive the Agulhas
 431 frontal dynamics and variability. Comparisons between the SAGE data and the model show
 432 that they captured the same frontal dynamics despite their respective limitations.

433 5 Spatial and Temporal variability of the instability

434 In this section we aim to better characterize the barotropic instability spatial and time
 435 variability.

436 5.1 Spatial variability of the instability

437 5.1.1 Where does barotropic instability occur along the Agulhas front ?

438 To investigate where the barotropic instability is triggered along the front, we determine
 439 the contribution of \overline{HRS} to the spatial evolution of \overline{EKE} . If \overline{HRS} is the main source of
 440 \overline{EKE} (Figures 10 and 11), the \overline{EKE} equation (Eq. 2) reduces at first order to :

$$\frac{D\overline{EKE}}{Dt} \equiv \bar{u} \partial_x \overline{EKE} \equiv \overline{HRS} \quad (3)$$

441 with u the along-front velocity component, x the corresponding direction and the overbar
 442 denoting a five-month time average when no Natal Pulse is present. The contribution of
 443 \overline{HRS} to the along-front evolution of \overline{EKE} is estimated from $\int_0^x \frac{\overline{HRS}}{\bar{u}} dx$ and compared to
 444 the full \overline{EKE} (Figure 13a).

445 Even though the mean energy conversion rate \overline{HRS} is positive over the Agulhas inshore
 446 front from 28°E to 23°E (Figures 10 and 11), the submesoscale eddies develop preferentially
 447 over a specific portion: between 28°E and 26°E (Figures 7a and b). This specific portion
 448 is also visible from the along-front distributions of \overline{EKE} and of the energy conversion rates
 449 HRS and VBF (Figure 13a).

450 Between 29°E and 25.5°E, \overline{HRS} is the dominant term responsible for the \overline{EKE} genera-
 451 tion and drives its along-front variations. The approximation: $\overline{EKE} \approx \int_0^x \frac{\overline{HRS}}{\bar{u}} dx$ is here
 452 valid. \overline{HRS} has positive values almost monotonously increasing and the \overline{EKE} is strongly
 453 increasing. Both patterns reflect the recurrent formation of vortex streets between 28°E
 454 and 26°E (Figures 7a and b) and their downstream advection.

455 Westward of Port Elizabeth (26°E), a combination of barotropic and baroclinic pro-
 456 cesses are responsible for the \overline{EKE} generation, but they combine with other processes acting
 457 as sinks of \overline{EKE} . At first order, the evolution of \overline{EKE} still follows the pattern of \overline{HRS} .

458 \overline{HRS} decreases to zero from 26°E to 25°E and, as a result, \overline{EKE} is flatter between 25.5°E
459 and 24.5°E . Downstream of 24.5°E , \overline{HRS} increases strongly again and \overline{VBF} becomes pos-
460 itive and increases as well. Both terms reach a maximum at 23.5°E . Accordingly, \overline{EKE}
461 increases strongly between 24.5°E and 23.5°E . However, \overline{EKE} does not increase as strongly
462 as suggested by the \overline{HRS} and \overline{VBF} terms ($EKE < \int_0^x \frac{\overline{HRS} + \overline{VBF}}{\overline{u}} dx$) as other processes
463 acting as \overline{EKE} sinks are also at play. Sinks include effects of the bottom friction, wind
464 stress, interior vertical mixing, horizontal diffusion, and of the nonlinear terms (Eq. 2) ad-
465 vecting \overline{EKE} out of the integration domain. Along this second front portion the flow still
466 gains \overline{EKE} , but some is also strongly dissipated. This indicates a dynamical shift of the
467 current towards a more turbulent nature.

468 This dynamical shift of the Agulhas current at 26°E is related to a topographical shift.
469 The eastern margin of the Agulhas Bank, which begins westward of 26°E , is associated
470 with an abrupt topography change including a sudden widening of the shelf break and
471 a curving of the topography (Figure 1). When reaching the eastern Agulhas Bank, the
472 current is known to increasingly meander in the mesoscale range (Lutjeharms, 2006; Paldor
473 & Lutjeharms, 2009; Krug et al., 2014). This is reflected in the evolution of the vortex
474 street. The modeled submesoscale eddies grow in size, potentially interact with each other
475 and dissipate. Other perturbations, such as Shear-Edge eddies, are known to grow and
476 occasionally leak downstream (Lutjeharms et al., 1989, 2003; Lutjeharms, 2006). To sum
477 up, when flowing close to the topography (upstream of 26°E) the barotropic instability leads
478 to submesoscale eddy generation. When the Agulhas Current is in a non-meandering state
479 they are the only \overline{EKE} source. When the topographic constraint relaxes on the current
480 (downstream of 26°E), the current develops meanders in the mesoscale range. The \overline{EKE}
481 sources are shared between barotropic and baroclinic processes and sinks also come into
482 play.

483 The triggering of the barotropic instability between 28°E and 26°E is associated with
484 intense relative vorticity upstream. Barotropic instability extracts energy from the mean
485 horizontal shear. In the context of the upstream Agulhas Current, the main contribution
486 to the horizontal shear is the lateral shear: $\partial_y \bar{u}$ (Figure 11). This term is also the main
487 contributor to the current's relative vorticity. Cross-front maxima of relative vorticity, for
488 different depths between the surface and 75 m, are plotted along the Agulhas front on Figure
489 13b. The relative vorticity is more intense at the surface than at depth. It suggests that
490 the front is more unstable at the very surface. This is coherent with \overline{HRS} being more
491 intense between the surface and 50 m depth (Figure 10) and the submesoscale eddies being
492 surface-intensified (Figures 8a and b).

493 The along-front relative vorticity provides an indication of where barotropic instability
494 can be triggered and lead to submesoscale eddy generation. Upstream of the location of
495 the barotropic instability triggering (28°E), the relative vorticity is the largest, with values
496 of about $O(6f)$ at the surface, indicative of a potentially unstable front. Downstream of
497 28°E , the relative vorticity decreases in two steps. Where the submesoscale eddies develop
498 (between 28°E and 26°E) the relative vorticity starts to decrease. Submesoscale eddies
499 induce meanders in the front and in doing so they spread the mean frontal relative vorticity.
500 The spread is the strongest at the surface where the submesoscale eddies are the most
501 intense. Westward of 26°E , the relative vorticity decreases, with values $O(< f)$, and becomes
502 vertically homogeneous. This decrease is due to the formation of Agulhas frontal meanders
503 of larger scales, downstream of Port Elizabeth (26°E) where the topography constraint on
504 the current is relaxed.

505 **5.1.2 What controls the triggering of the barotropic instability around 28°E ?**

506 The barotropic instability originates from an unstable shear, itself set by the background
 507 strain. The mean strain, $\frac{\bar{S}}{f}$, is defined as :

$$\left(\begin{array}{c} \partial_x \bar{u} - \partial_y \bar{v} \\ \partial_x \bar{v} + \partial_y \bar{u} \end{array} \right)$$

508 with u and v the velocity components in the x and y directions, f the Coriolis parameter
 509 and the overbar denoting a five-month time average when no Natal Pulse is present. The
 510 background strain reflects the large scale straining and stretching acting on the flow. It can
 511 actively intensify the velocity and the horizontal gradients of tracers if its axis is aligned
 512 with the frontal axis. Both axes are aligned if their angle is inferior to $\frac{\pi}{4}$ (Hoskins, 1982) and
 513 in that case the background strain is frontogenetic. Conversely, if the strain and the frontal
 514 axis are not aligned the strain spreads the front and is frontolytic. The Agulhas inshore
 515 front is associated with an intense background strain at 25 m depth (Figure 14). Upstream
 516 of 28°E, the strain is the strongest and is well aligned with the front, whereas downstream
 517 of 26°E, it is weaker and the strain and frontal axis alignment is lost. The along-front
 518 distribution of the mean relative vorticity (Figure 13b) originates from the combined effect
 519 of the strain magnitude and of its alignment with the frontal axis. The portion where the
 520 front is the most sheared (upstream of 28°E) is consistent with the background strain being
 521 the most efficient at sharpening and intensifying the Agulhas front.

522 The barotropic instability is triggered where the background strain weakens. Where the
 523 front destabilizes, downstream of 28°E, the alignment of the strain with the front decreases,
 524 meaning the strain is less efficient at driving the front intensification. A frontogenetic back-
 525 ground strain has the conjoint effect of intensifying the front and preventing mean horizontal
 526 shear-related instabilities to be triggered. In doing so it "stabilizes" a potentially unstable
 527 2D relative vorticity band (Dritschel et al., 1991). Similarly, a frontogenetic tendency can
 528 prevent the triggering of shear instabilities on the upstream face of a Gulf Stream frontal
 529 eddy (Gula et al., 2016a), as well as the development of submesoscale cross-front disturbances
 530 on the upstream face of jet meandering troughs (McWilliams et al., 2019). By stretching
 531 and straining the front, the background strain exerts a stress in the along-front direction
 532 which inhibits any cross-front momentum and energy transfer. To sum up, the barotropic
 533 instability develops just downstream of a front portion where the relative vorticity is the
 534 most intense. This large relative vorticity originates from a frontogenetic background strain.
 535 The instability triggering is concomitant with the background strain weakening. When the
 536 front is released from the background strain constraint there is no external stress restraining
 537 the development of cross-frontal features and the front destabilizes.

538 A frontogenetic background strain usually results from the combination of the back-
 539 ground mesoscale advection field and of the topographic constraint on the flow. Several
 540 studies connect front destabilizations with a weakening of the background strain (Mole-
 541 maker et al., 2015; Gula et al., 2015b). In these studies, a straight and steep topography
 542 is identified to be at the origin of an intense background strain which is reinforced by the
 543 effect of the topographic drag on the current shear. An abrupt separation of the current
 544 from the topography leads to the strain weakening and thus to the triggering of barotropic
 545 instabilities just downstream the separation.

546 The Agulhas Current case differs slightly. The instability is triggered along a front
 547 portion where the current flows closely to the topography. In fact, the topographic constraint
 548 on the flow relaxes further downstream (at Port Elizabeth 26°E). The triggering of the
 549 barotropic instability between 28°E and 26°E is thus not directly related to a topographic
 550 change. This mismatch between the front dynamics and the topographic constraint is also
 551 visible from the vertical structure of the strain (not shown here). Similarly to the relative
 552 vorticity (Figure 11), the strain is the strongest at the surface even though along this portion
 553 of the front, the front is not in contact with the topography at depths shallower than 150-
 554 200 m (not shown here). Therefore the background mesoscale advection field would be the

555 main contributor to the intense background strain at the surface. The contribution of the
 556 topography in the front intensification and destabilization between 28°E and 26°E in the
 557 submesoscale range is less evident.

558 5.2 Time variability of the instability

559 While submesoscale eddy generation by barotropic instability is a recurrent process
 560 (Figures 11 and 12), which drives the Agulhas front variability in the submesoscale range
 561 in the vicinity of Port Elizabeth (26°E), it is an intermittent process with a strong time
 562 variability.

563 The Agulhas front variability at relatively high frequencies is investigated with a five-
 564 month long time series of the energy conversion term *HRS* (Figure 12). The time series is
 565 built with the *HRS* term averaged over the vertical and over the frontal area between 28°E
 566 and 26°E from July to November when no Natal Pulse is present. Hence, this time series
 567 takes place during the austral winter, when Krug & Tournadre (2012); Beal et al. (2015)
 568 observed the current to be less intense.

569 Submesoscale eddy generation shows a periodicity of about 10 days, on average, from
 570 the *HRS* time series. The *HRS* time series shows a constantly positive fluctuating signal
 571 (Figure 15). Not all the *HRS* peaks correspond to submesoscale eddy generation and ten
 572 events of actual submesoscale eddy generation are identified from a surface relative vorticity
 573 movie. They are marked in shades of grey on the *HRS* time series. These events are spaced
 574 by about 10 days on average. This periodicity also comes out from a five-month long time
 575 series of the surface relative vorticity upstream of the instability triggering location (28°E)
 576 (not shown here). The triggering of the barotropic instability is then connected to the
 577 fluctuations, with a 10 days period, of the Agulhas inshore front structure.

578 The submesoscale eddy generation periodicity is relatively close to the Agulhas Current
 579 and to the Agulhas Undercurrent's ones. Bryden et al. (2005) and Beal (2009) respectively
 580 looked at the Agulhas Current and Agulhas Undercurrent time variability using 12 and a 17
 581 month-long *in situ* records of current velocity. They show that both currents have the largest
 582 variability for the Natal Pulse period (60 days). At lower periods the Agulhas Current shows
 583 a large variability for periods between 8-27 days and the Agulhas Undercurrent for periods
 584 of 25 days and between 8-20 days. The variability of the submesoscale eddy generation is
 585 associated with large scale variations of the Agulhas Current and Undercurrent rather than
 586 with local variations of the Agulhas inshore front.

587 The few listed possible mechanisms involved in the time variability of the submesoscale
 588 eddy generation are a remote and a local forcings : the Coastal Trapped Waves or Rossby
 589 Topographic Waves and the wind stress respectively. Schumann & Brink (1990) showed,
 590 from *in situ* measurements of sea level along the Southern African coastline, that Coastal
 591 Trapped Waves affect the South African continental shelf dynamics and possibly interact
 592 with the Agulhas Current upstream of Port Elizabeth. Even though no study investigated
 593 the Rossby Topographic Waves along the South African continental slope, the location where
 594 the submesoscale eddies develop (28-26°E) is favourable to their development in theory.
 595 Both waves can affect the Agulhas inshore front dynamics and then be involved or interact
 596 with the submesoscale eddies.

597 Rather than one process setting the conditions for the instability to be triggered, this
 598 can be the result of a combination of different processes all acting to destabilize the front.
 599 Local wind is another possible factor impacting the frontal dynamics. Thomas & Lee (2005)
 600 showed that down-front winds induce an Ekman transport of dense waters in the top of light
 601 waters resulting in the frontogenetic process enhancement. Schaeffer et al. (2017) observed
 602 the Eastern Australian Current mainly meandered and destabilized under up-front winds
 603 conditions leading to the formation of submesoscale frontal cyclonic eddies. However, in
 604 this study local wind forcing is not favourable before and during the submesoscale eddy

generation. In this section we address the spatial and time variability of the barotropic instability triggering. The barotropic instability triggering in the submesoscale range and leading to the generation of frontal submesoscale eddies is the only source of variability for the Agulhas inshore front in the absence of Natal Pulses. The instability originates from an intense relative vorticity at the surface which itself is driven by the frontogenetic background strain. However, the relative contributions of the topography and of the background mesoscale advection field on driving the background strain are not completely disentangled and need further investigations. In the same way, further studies are needed to determine in which proportion remote and local mechanisms contribute to the 10 days variability of the instability triggering.

6 Conclusion

Our study addresses the Agulhas Current frontal dynamics in the submesoscale range. We investigated and characterized the generation mechanism of frontal submesoscale eddies along a non-meandering Agulhas Current using a high-resolution ($dx \sim 0.75$ km) numerical simulation. The simulation reproduces frontal cyclonic submesoscale eddies in the vicinity of Port Elizabeth (26°E) with a diameter range of 10-20 km in agreement with satellite and *in situ* observations.

A 1D linear stability analysis, of the cross-front shear upstream of the instability triggering location (28°E) shows that it is barotropically unstable and it develops perturbations with wavelengths of 10-13 km matching the scale of the submesoscale eddies. Barotropic instability is confirmed as the simulated submesoscale eddy generation mechanism by an energy transfer analysis. The barotropic instability is a horizontal shear instability which draws its energy from the mean kinetic energy field when the mean horizontal shear is unstable ($\overline{HRS} = MKE \rightarrow EKE$). Comparison between the modeled barotropic instabilities and the ones observed during SAGE shows that the lateral shear is the main contribution to the energy conversion term \overline{HRS} .

Our energy transfer analysis over longer time periods (one and five-month long) indicates that the submesoscale frontal eddy generation by barotropic instability is a recurrent process which drives most of the variability around Port Elizabeth (26°E).

This result gives new insights on the Agulhas Current along-stream dynamics. When considering a broader scale range, from the mesoscale to the submesoscale, the current dynamics are less dichotomous than previously described (Lutjeharms, 2006; Paldor & Lutjeharms, 2009).

This study shows that in addition to the Natal Pulses (mesoscale solitary meanders), frontal submesoscale eddies also locally drive the "stable" branch variability around Port Elizabeth (26°E). Rather than a dynamical shift, Port Elizabeth is the location of a smooth transition, between a "stable" and an "unstable" branch in the mesoscale range, via the triggering of instabilities in the submesoscale range. Hence, the so far known sources of variability for the upstream "stable" branch are the Natal Pulses and the frontal submesoscale eddies which both originate from barotropic instability (Biastoch & Krauss, 1999; Tsugawa & Hasumi, 2010; Beal et al., 2015).

The spatial variability of the barotropic instability triggering originates from the background strain. Between 28°E and 26°E , barotropic instability is triggered and leads to the generation of frontal submesoscale eddies. Upstream of the instability triggering location (28°E), the background strain is frontogenetic and the front is intensively sheared. The frontogenetic strain has the double effect of intensifying the shear and of preventing the development of cross-frontal perturbations. Downstream, the frontogenetic influence of the strain weakens allowing for barotropic instability to be triggered along the front.

653 The origin of the frontogenetic background strain slightly differs between the Agulhas
 654 Current and the Gulf Stream. The bottom friction does not play a leading role in generating
 655 the current's horizontal shear and the topographic constraint role is not as evident as in the
 656 Gulf Stream (Gula et al., 2015b).

657 The triggering of barotropic instability has a periodicity of about 10 days on average.
 658 Possible mechanisms driving this time variability are Coastal Trapped Waves or Rossby
 659 Topographic Waves and wind stress. Their relative contributions need further investigation.

660 The submesoscale frontal eddies could drive exchanges of material and momentum
 661 between shelf waters and the Agulhas Current, with potential consequences on coastal dy-
 662 namics, marine life and large scale circulation. Additional observations and modeling studies
 663 are required to address these aspects.

664 Acknowledgments

665 This work was granted access to the HPC resources of IDRIS under the allocation A0040107630
 666 made by GENCI at Paris, France and of the HPC facilities DATARMOR of "Pôle de Calcul
 667 Intensif pour la Mer" at Ifremer, Brest, France. Model outputs are available upon request.
 668 This work was supported by the RADII funding as well as Ifremer and the Brittany re-
 669 gion for PhD funding. Odyssea Regional South Africa products are available at <http://www.ifremer.fr/opendap/cerdap1/ghrsst/14/saf/odyssea-nrt/data> and MODIS SST
 670 data are available (Level 4) at <http://cersat.ifremer.fr/data/products/catalogue>.
 671 The drifter datasets ANDRO and NOAA are respectively available at <https://www.umr-lops.fr/Donnees/ANDRO> and <https://www.aoml.noaa.gov/phod/gdp/interpolated/data/subset.php>. The AVISO data are available at <ftp.aviso.altimetry.fr>. Gridded cross-
 672 sectional velocities are based on *in situ* current meter measurements from the Agulhas Cur-
 673 rent Time-series (ACT) experiment (Beal et al., 2015) and can be downloaded at <https://beal-agulhas.rsmas.miami.edu/data-and-products/index.html>. We, as well, want to
 674 especially thank Heather Reagan for her precious help in correcting the manuscript language.

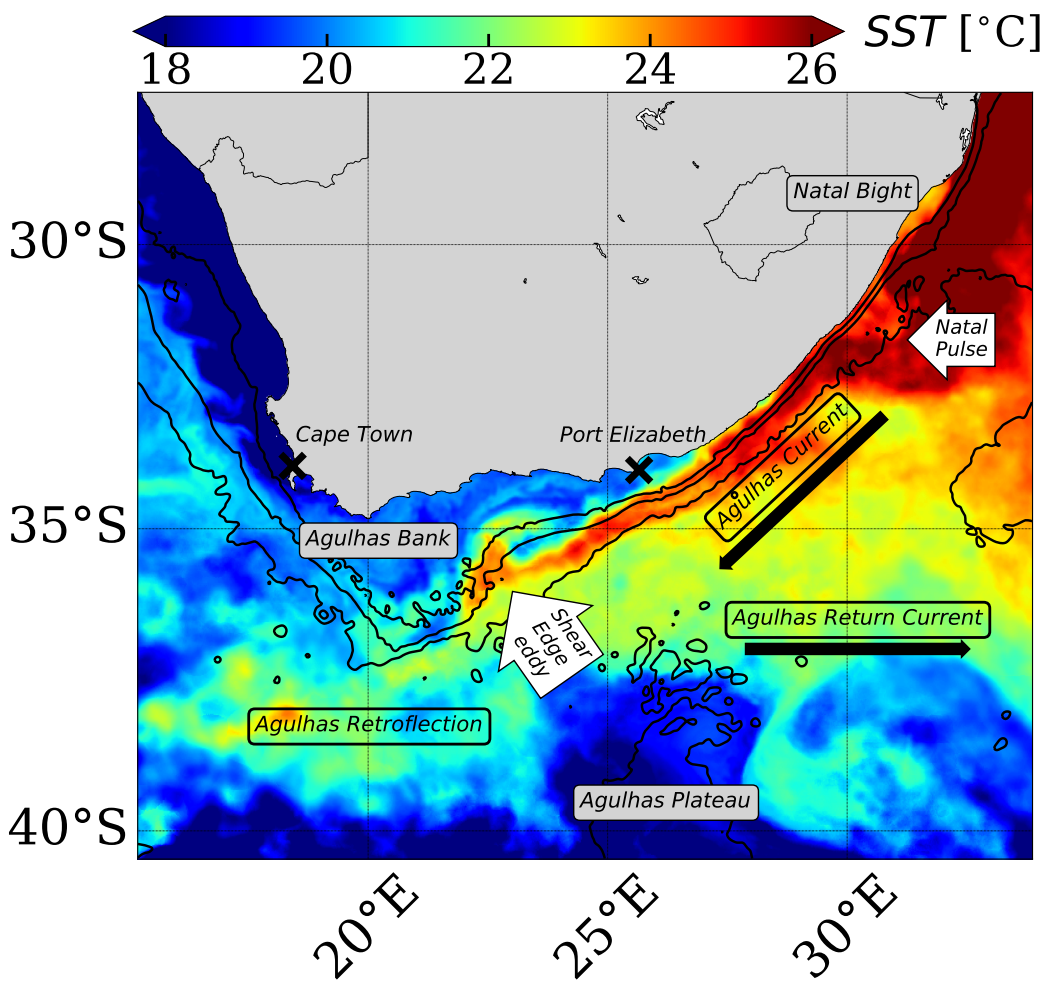
675 References

- 680 Beal, L. (2009). A time series of Agulhas Undercurrent transport. *Journal of physical*
 681 *oceanography*, 39(10), 2436–2450.
- 682 Beal, L., De Ruijter, W., Biastoch, A., & Ringer, Z. (2011). On the role of the Agulhas
 683 system in ocean circulation and climate. *Nature*, 472, 429–436.
- 684 Beal, L., Eliop, S., Houk, A., & Leber, G. (2015). Capturing the transport variability of a
 685 western boundary jet: Results from the Agulhas Current Time-Series Experiment (ACT).
Journal of Physical Oceanography, 45(5), 1302–1324.
- 686 Beckmann, A., & Haidvogel, D. (1993). Numerical simulation of flow around a tall iso-
 687 lated seamount. Part I: Problem formulation and model accuracy. *Journal of Physical*
Oceanography, 23(8), 1736–1753.
- 688 Biastoch, A., & Krauss, W. (1999). The role of mesoscale eddies in the source regions of
 689 the Agulhas Current. *Journal of Physical Oceanography*, 29(9), 2303–2317.
- 690 Bryden, H., Beal, L., & Duncan, L. (2005). Structure and transport of the Agulhas Current
 691 and its temporal variability. *Journal of Oceanography*, 61(3), 479–492.
- 692 Chelton, D., Deszoeke, R., Schlax, M., Naggar, K. E., & Siwertz, N. (1998). Geograph-
 693 ical variability of the first baroclinic Rossby radius of deformation. *Journal of Physical*
Oceanography, 28(3), 433–460.
- 694 Chelton, D., Schlax, M., & Samelson, R. (2011). Global observations of nonlinear mesoscale
 695 eddies. *Progress in oceanography*, 91(2), 167–216.
- 696 Debreu, L., Marchesiello, P., Penven, P., & Chambon, G. (2012). Two-way nesting in split-
 697 explicit ocean models: Algorithms, implementation and validation. *Ocean Modelling*,
 698 49–50, 1–21.

- 702 Dee, D., Uppala, S., Simmons, A., Berrisford, P., Poli, P., Kobayashi, S., ... others (2011).
 703 The ERA-Interim reanalysis: Configuration and performance of the data assimilation
 704 system. *Quarterly Journal of the royal meteorological society*, *137*(656), 553–597.
- 705 Dritschel, D., Haynes, P., Juckes, M., & Shepherd, T. (1991). The stability of a two-
 706 dimensional vorticity filament under uniform strain. *Journal of Fluid Mechanics*, *230*,
 707 647–665.
- 708 Durski, S., Glenn, S., & Haidvogel, D. (2004). Vertical mixing schemes in the coastal ocean:
 709 Comparison of the level 2.5 Mellor-Yamada scheme with an enhanced version of the K
 710 profile parameterization. *Journal of Geophysical Research: Oceans*, *109*(C1).
- 711 Elipot, S., & Beal, L. M. (2015). Characteristics, Energetics, and Origins of Agulhas
 712 Current Meanders and Their Limited Influence on Ring Shedding. *Journal of Physical*
 713 *Oceanography*, *45*(9), 2294–2314. doi: 10.1175/JPO-D-14-0254.1
- 714 Fairall, C., Bradley, E., Rogers, D., Edson, J., & Young, G. (1996). Bulk parameterization
 715 of air-sea fluxes for tropical ocean-global atmosphere coupled-ocean atmosphere response
 716 experiment. *Journal of Geophysical Research: Oceans*, *101*(C2), 3747–3764.
- 717 Ferrari, R., & Wunsch, C. (2010). The distribution of eddy kinetic and potential energies
 718 in the global ocean. *Tellus A: Dynamic Meteorology and Oceanography*, *62*(2), 92–108.
- 719 Ferry, N., Parent, L., Garric, G., Bricaud, C., Testut, C., Galloudec, O. L., ... others
 720 (2012). Glorys2v1 global ocean reanalysis of the altimetric era (1992–2009) at meso scale.
 721 *Mercator Ocean-Quaterly Newsletter*, *44*.
- 722 Gula, J., Molemaker, M., & McWilliams, J. (2014). Submesoscale cold filaments in the Gulf
 723 Stream. *J. Phys. Oceanogr.*, *44*(10), 2617–2643.
- 724 Gula, J., Molemaker, M., & McWilliams, J. (2015a). Gulf Stream dynamics along the
 725 Southeastern U.S. Seaboard. *J. Phys. Oceanogr.*, *45*(3), 690–715.
- 726 Gula, J., Molemaker, M., & McWilliams, J. (2015b). Topographic vorticity generation,
 727 submesoscale instability and vortex street formation in the Gulf Stream. *Geophys. Res.*
 728 *Lett.*, *42*, 4054–4062. doi: 10.1002/2015GL063731
- 729 Gula, J., Molemaker, M., & McWilliams, J. (2016a). Submesoscale dynamics of a Gulf
 730 Stream frontal eddy in the South Atlantic Bight. *Journal of Physical Oceanography*,
 731 *46*(1), 305–325.
- 732 Gula, J., Molemaker, M., & McWilliams, J. (2016b). Topographic generation of subme-
 733 soscale centrifugal instability and energy dissipation. *Nature communications*, *7*, 12811.
- 734 Haidvogel, D., & Beckmann, A. (1999). *Numerical ocean circulation modeling*. World
 735 Scientific.
- 736 Halo, I., Backeberg, B., Penven, P., Ansorge, I., Reason, C., & Ullgren, J. (2014). Eddy prop-
 737 erties in the Mozambique Channel: A comparison between observations and two numerical
 738 ocean circulation models. *Deep Sea Research Part II: Topical Studies in Oceanography*,
 739 *100*, 38–53.
- 740 Hoskins, B. J. (1982). The mathematical theory of frontogenesis. *Annual review of fluid*
 741 *mechanics*, *14*(1), 131–151.
- 742 Krug, M., Swart, S., & Gula, J. (2017). Submesoscale cyclones in the Agulhas Current.
 743 *Geophys. Res. Lett.*, *44*.
- 744 Krug, M., & Tournadre, J. (2012). Satellite observations of an annual cycle in the Agulhas
 745 Current. *Geophysical Research Letters*, *39*(15).
- 746 Krug, M., Tournadre, J., & Dufois, F. (2014). Interactions between the Agulhas Current
 747 and the eastern margin of the Agulhas Bank. *Continental Shelf Research*, *81*, 67–79.
- 748 Large, W. G., & Yeager, S. (2004). Diurnal to decadal global forcing for ocean and sea-ice
 749 models: the data sets and flux climatologies.
- 750 Lemarié, F., Kurian, J., Shchepetkin, A., Molemaker, M., Colas, F., & McWilliams, J.
 751 (2012). Are there inescapable issues prohibiting the use of terrain-following coordinates
 752 in climate models? *Ocean Modelling*, *42*, 57–79.

- 756 Lutjeharms, J. (2006). *The Agulhas Current* (Vol. 2). Springer.
- 757 Lutjeharms, J., Catzel, R., & Valentine, H. (1989). Eddies and other boundary phenomena
758 of the Agulhas Current. *Continental Shelf Research*, 9(7), 597–616.
- 759 Lutjeharms, J., & Gordon, A. (1987). Shedding of an Agulhas ring observed at sea. *Nature*,
760 325(6100), 138.
- 761 Lutjeharms, J., Penven, P., & Roy, C. (2003). Modelling the shear edge eddies of the
762 southern agulhas current. *Continental Shelf Research*, 23(11-13), 1099–1115.
- 763 Mahadevan, A. (2014). Ocean science: Eddy effects on biogeochemistry. *Nature*, 506(7487),
764 168.
- 765 Marchesiello, P., Debreu, L., & Couvelard, X. (2009). Spurious diapycnal mixing in terrain-
766 following coordinate models: The problem and a solution. *Ocean Modelling*, 26(3-4),
767 156–169.
- 768 McWilliams, J. C., Gula, J., & Molemaker, M. J. (2019). The Gulf Stream North Wall:
769 Ageostrophic Circulation and Frontogenesis. *Journal of Physical Oceanography*, 49(4),
770 893–916.
- 771 Méneguen, C., McWilliams, J., & Molemaker, M. (2012). Ageostrophic instability in a
772 rotating stratified interior jet. *Journal of fluid mechanics*, 711, 599–619.
- 773 Molemaker, M., McWilliams, J., & Dewar, W. (2015). Submesoscale instability and gener-
774 ation of mesoscale anticyclones near a separation of the California Undercurrent. *Journal of
775 Physical Oceanography*, 45(3), 613–629.
- 776 Paldor, N., & Lutjeharms, J. (2009). Why is the stability of the Agulhas Current geo-
777 graphically bi-modal? *Geophysical Research Letters*, 36(14), n/a–n/a. Retrieved from
778 <http://dx.doi.org/10.1029/2009GL038445> (L14604) doi: 10.1029/2009GL038445
- 779 Peeters, F., Acheson, R., Brummer, G.-J., De Ruijter, W., Schneider, R., Ganssen, G., ...
780 Kroon, D. (2004). Vigorous exchange between the Indian and Atlantic oceans at the end
781 of the past five glacial periods. *Nature*, 430(7000), 661.
- 782 Penven, P., Lutjeharms, J., Marchesiello, P., Roy, C., & Weeks, S. (2001). Generation of cy-
783 clonic eddies by the Agulhas Current in the Lee of the Agulhas Bank. *Geophysical Research
784 Letters*, 28(6), 1055–1058. Retrieved from <http://dx.doi.org/10.1029/2000GL011760>
785 doi: 10.1029/2000GL011760
- 786 Renault, L., McWilliams, J., & Penven, P. (2017). Modulation of the Agulhas Current
787 Retroflection and Leakage by Oceanic Current Interaction with the Atmosphere in Cou-
788 pled Simulations. *Journal of Physical Oceanography*, 47(8), 2077–2100.
- 789 Rouault, M., & Penven, P. (2011). New perspectives on Natal Pulses from satellite obser-
790 vations. *Journal of Geophysical Research: Oceans*, 116(C7), n/a–n/a. Retrieved from
791 <http://dx.doi.org/10.1029/2010JC006866> (C07013) doi: 10.1029/2010JC006866
- 792 Schaeffer, A., Gramouille, A., Roughan, M., & Mantovanelli, A. (2017). Characterizing
793 frontal eddies along the East Australian Current from HF radar observations. *Journal of
794 Geophysical Research: Oceans*, 122(5), 3964–3980.
- 795 Schouten, M., De Ruijter, W., & Van Leeuwen, P. (2002). Upstream control of Agulhas
796 Ring shedding. *Journal of Geophysical Research: Oceans*, 107(C8), 23–1.
- 797 Schumann, E., & Brink, K. (1990). Coastal-trapped waves off the coast of south africa:
798 generation, propagation and current structures. *Journal of Physical Oceanography*, 20(8),
799 1206–1218.
- 800 Schumann, E., & Van Heerden, I. (1988). Observations of Agulhas Current frontal features
801 south of Africa, October 1983. *Deep Sea Research Part A. Oceanographic Research Papers*,
802 35(8), 1355–1362.
- 803 Shchepetkin, A., & McWilliams, J. (2005). The Regional Oceanic Modeling System
804 (ROMS): A split-explicit, free-surface, topography-following- coordinate ocean model.
805 *Ocean Modelling*, 9, 347-404.
- 806 Soufflet, Y., Marchesiello, P., Lemarié, F., Jouanno, J., Capet, X., Debreu, L., & Benshila,
807 R. (2016). On effective resolution in ocean models. *Ocean Modelling*, 98, 36–50.
- 808 Thomas, L., & Lee, C. (2005). Intensification of ocean fronts by down-front winds. *Journal
809 of Physical Oceanography*, 35(6), 1086–1102.

- 810 Tsugawa, M., & Hasumi, H. (2010). Generation and growth mechanism of the natal pulse.
 811 *Journal of Physical Oceanography*, 40(7), 1597–1612.
- 812 Weijer, W., De Ruijter, W., Sterl, A., & Drijfhout, S. (2002). Response of the Atlantic
 813 Overturning Circulation to South Atlantic sources of buoyancy. *Global and Planetary
 814 Change*, 34(3-4), 293–311.



15 **Figure 1.** Snapshot of the Sea Surface Temperature (SST) [$^{\circ}$ C] on the 04-June-2014 from the
 16 Odyssea Regional South African product, showing the warm Agulhas Current extending from the
 17 southern boundary of the Mozambique Channel to the retroflexion and returning in the South
 18 Indian gyre as the Agulhas Return Current (black legends). The main topographic characteristics
 19 along the Agulhas path are displayed (grey legends). The thin black lines follow the 200 m, 1000
 20 m and 3000 m isobaths. Two perturbations, a Natal Pulse and a Shear-Edge eddy (white arrows)
 21 are developing along the Agulhas cyclonic front.

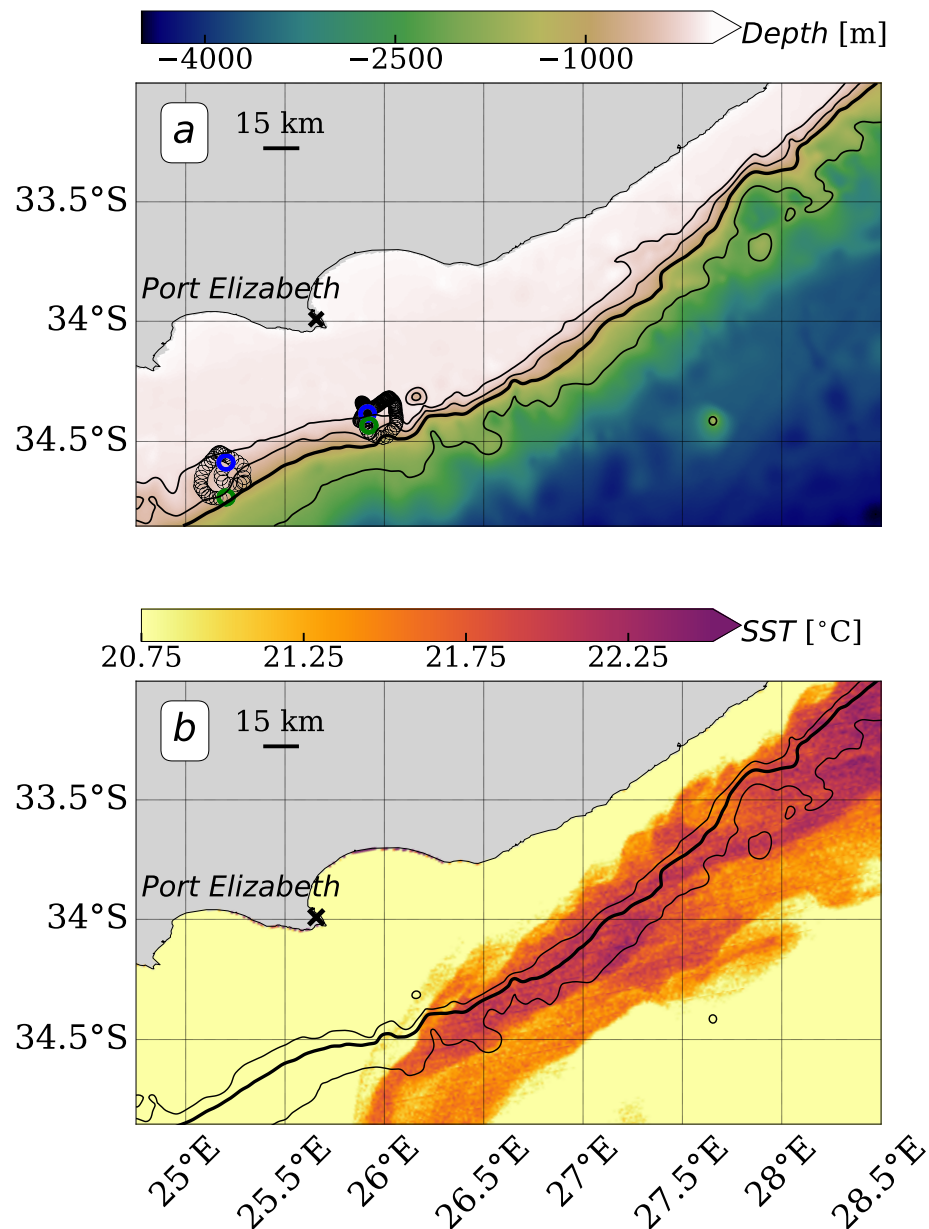


Figure 2. (a) Black circles track two Seagliders when they sampled two submesoscale cyclonic features between the 19-April and the 20-May 2015 (Krug et al., 2017). The first and last measures inside these features are respectively marked with green and blue circles. The background colors represent the bathymetry. The thin black lines follow the 200 m, 500 m and 2000 m isobaths. The bold black line is the 1000 m isobath, which corresponds to the Agulhas front location during the SAGE observations. (b) A snapshot of Sea Surface Temperature (SST) [$^{\circ}$ C], from the denoised Moderate-Resolution Imaging Spectroradiometer (MODIS) on the 19-July-2010. The black lines represent the same isobaths than in (a), except for the 200 m which is not represented. Submesoscale meanders develop upstream of Port Elizabeth, between 28.5° E and 26° E.

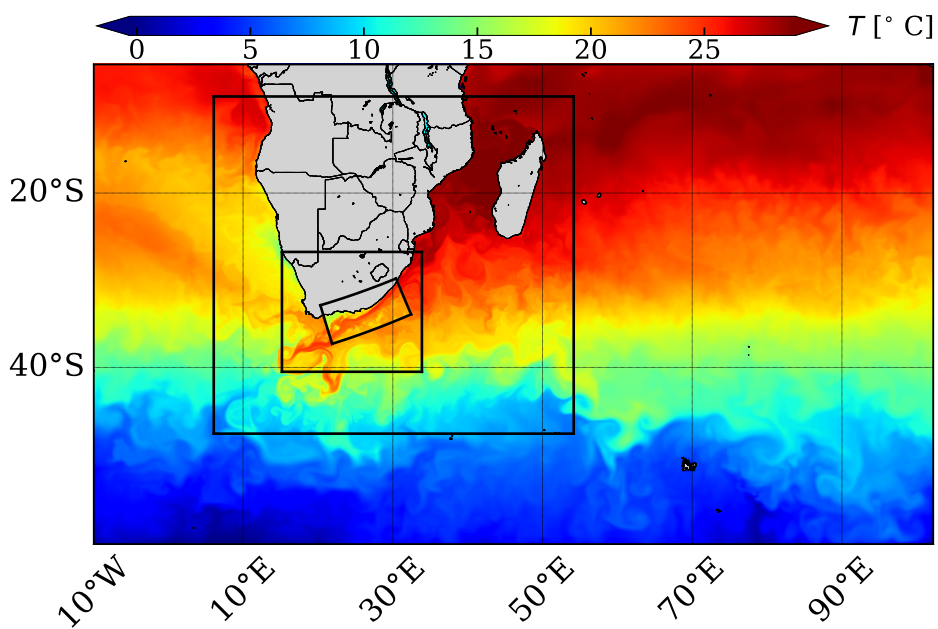


Figure 3. Snapshot of surface temperature [$^{\circ}\text{C}$] simulated by CROCO for the four nested domains : $\text{dx} \sim 22, 7.5, 2.5$ and 0.75 km .

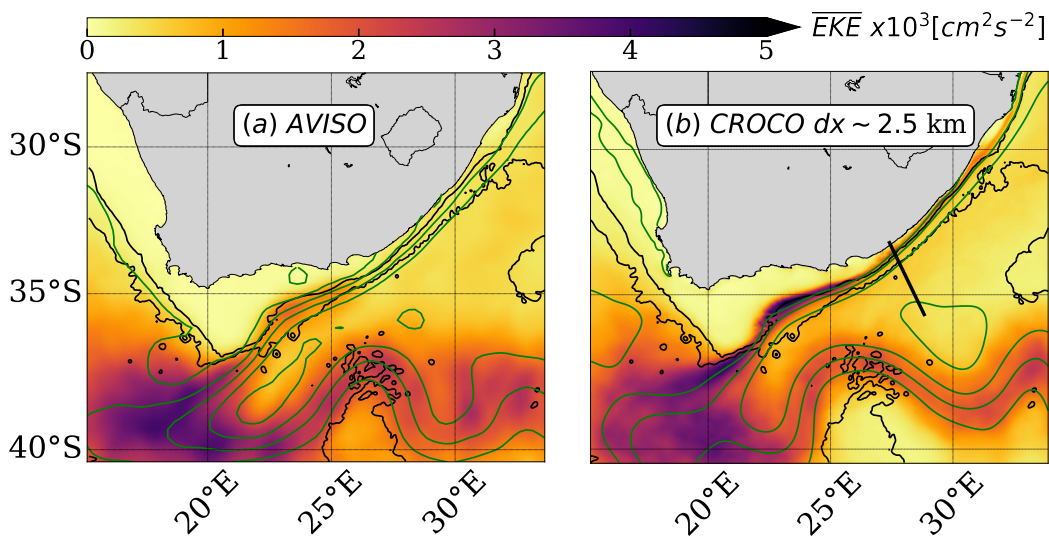
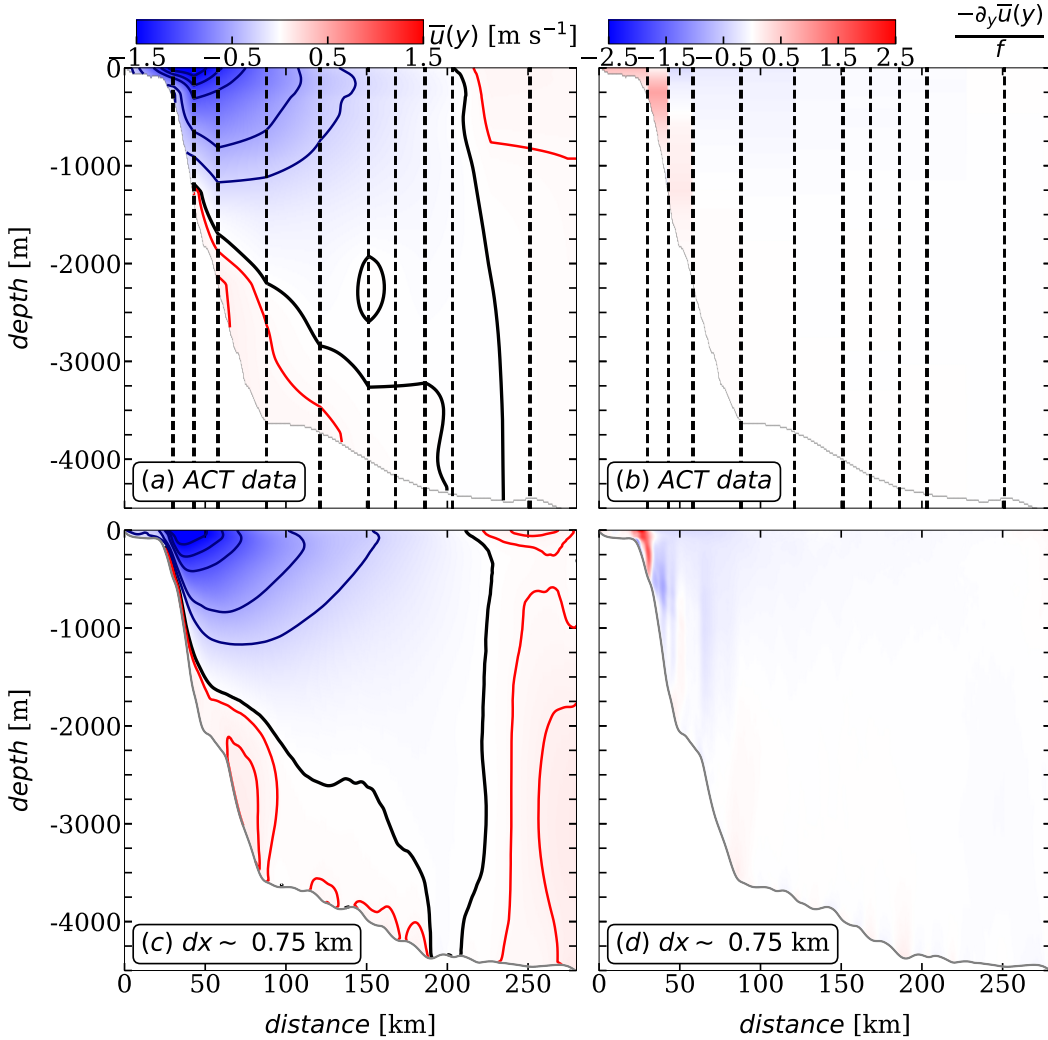


Figure 4. Maps of the mean surface \overline{EKE} [$\text{cm}^2 \text{s}^{-2}$] for (a) AVISO (1993-2003 period) and (b) CROCO at $\text{dx} \sim 2.5 \text{ km}$. Black contours are the 1000 m and 3000 m isobaths and green contours are the isolines of mean sea surface height between -2 and 2 m with a lag of 0.25 m. The black segment in Figure 4b shows the location of the vertical sections plotted along the ACT array in Figures 5. Both observed and modeled low ($O(0.5-2) 10^3 \text{ cm}^2 \text{s}^{-2}$) and large ($> O(3.5) 10^3 \text{ cm}^2 \text{s}^{-2}$) \overline{EKE} values along the upstream stable and downstream unstable Agulhas branches. The topography plays a role on the current dynamics and small scales (10-70 km) can locally drive the front variability.



Accepted Article

Figure 5. Sections of the mean along-front velocity ($\bar{u}(y)$ [m s⁻¹]) and mean normalized relative vorticity ($-\frac{\partial_y \bar{u}}{f}$) around 28.5°E derived from the ACT dataset (a and b) and the model at $dx \sim 0.75$ km (c and d). The location of the ACT array is shown by the black segment in Figure 4c. The black dashed lines locate the seven full-depths current meter moorings. The black cross indicates the 150 kHz ADCP at 300 m at the location of the first mooring. On the mean along-front velocity panels, the blue contours are the -0.25, -0.5, -1, -1.25 and -1.5 m s⁻¹ isolines, the red contours are the 0.03 and 0.08 m s⁻¹ isolines and the bold black contour is the 0 m s⁻¹ isoline. The observed and modeled mean vertical structures of the Agulhas Current show an intense cyclonic front expanding from the surface to 500 m.

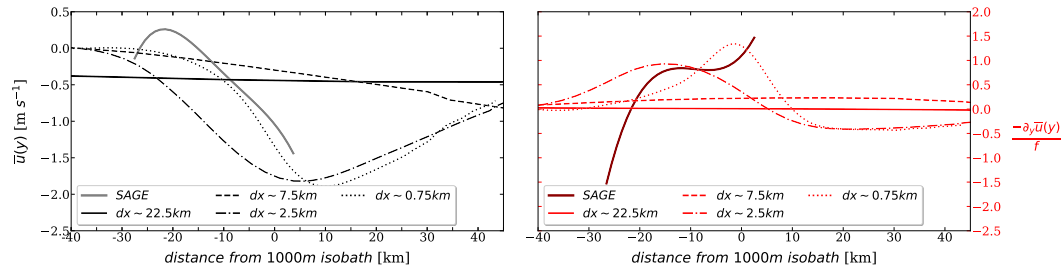


Figure 6. Cross-front sections of the mean along-front velocities ($\bar{u}(y)$ [m s⁻¹], on the left panel) and relative vorticity ($-\frac{\partial_y \bar{u}(y)}{f}$, on the right panel) at the SAGE location (25.75° E, shown in Figure 2a) for the SAGE glider data (Krug et al., 2017) (grey and dark red lines) and for the four model nests at $dx \sim 22.5$ (plain lines), 7.5 (dashed-dotted lines), 2.5 (dashed lines) and 0.75 km (dotted lines) resolution. The brackets denote the along-front average. The bottom x-axis represents the cross-front distance from the 1000 m isobath, which represents the front position for the SAGE period. The highest-resolution nest has a frontal structure close to the SAGE dataset.

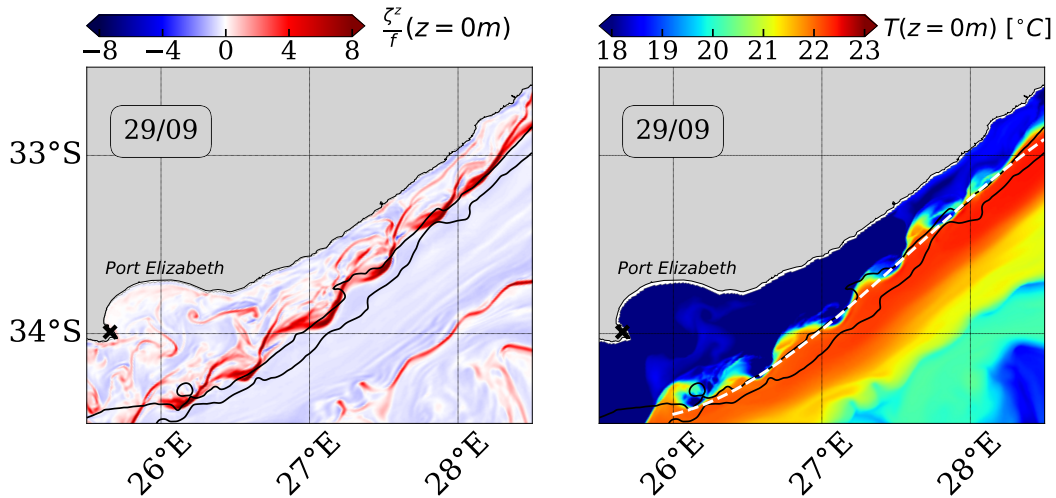


Figure 7. Snapshots of the surface normalized vertical relative vorticity ($\frac{\zeta^z}{f}$, on the left panel) and of the temperature (T [°C], on the right panel) when submesoscale eddies are present. Black contours are the 200 m and 1000 m isobaths. The white dashed line represents the location of the vertical sections plotted along the vortex street in Figures 8 and 10 bottom panel. The vortex street develops along the front between 28° E and 26° E.

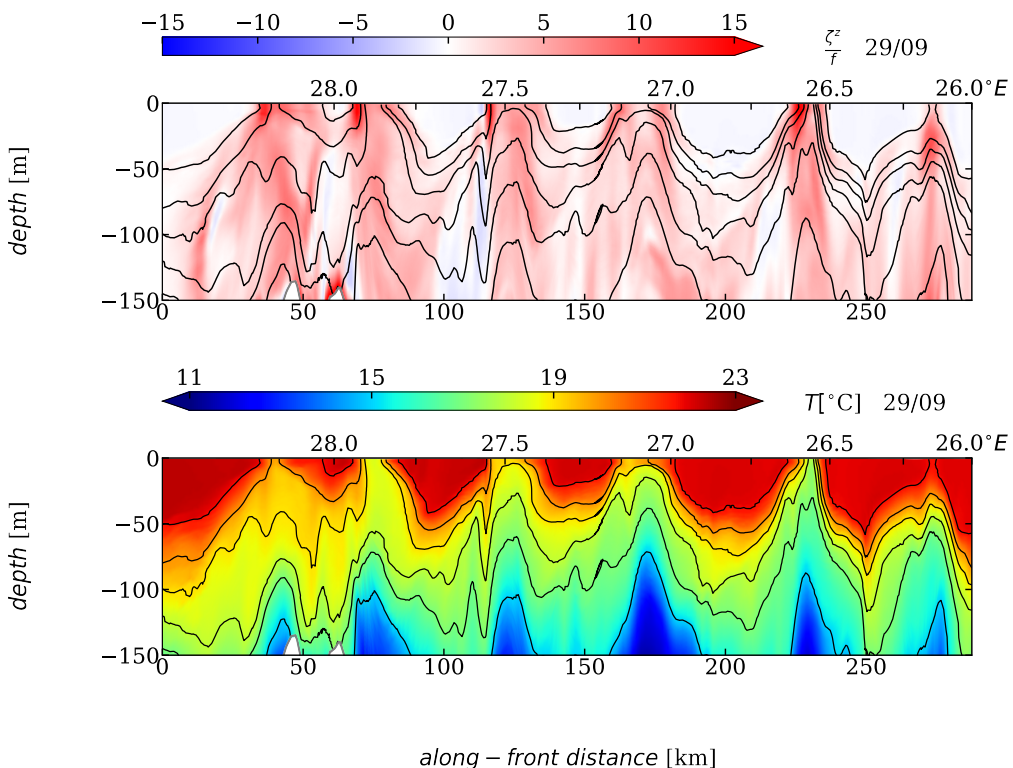


Figure 8. Sections along the vortex street, between 28.5°E and 26°E , plotted at the same time than in Figure 7. The sections are the normalized relative vorticity ($\frac{\zeta^z}{f}$, on the top panel) and the temperature ($T[\text{°C}]$, on the bottom panel). The black contours are the 15, 17, 18, 19, 20 and 21.75°C isotherms. The location of the sections along the vortex street is shown as the white dashed line in Figure 7. On the vertical, the submesoscale cyclonic eddies are surface-intensified with cold-cores and large relative vorticity values.

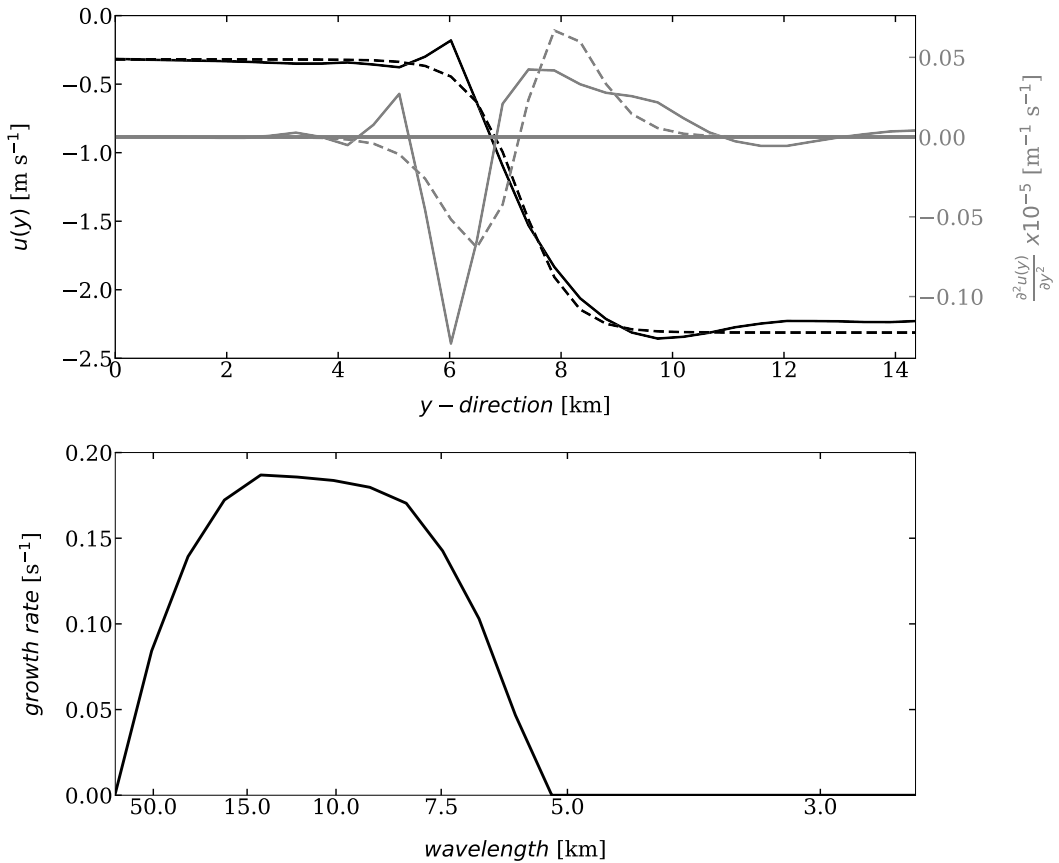
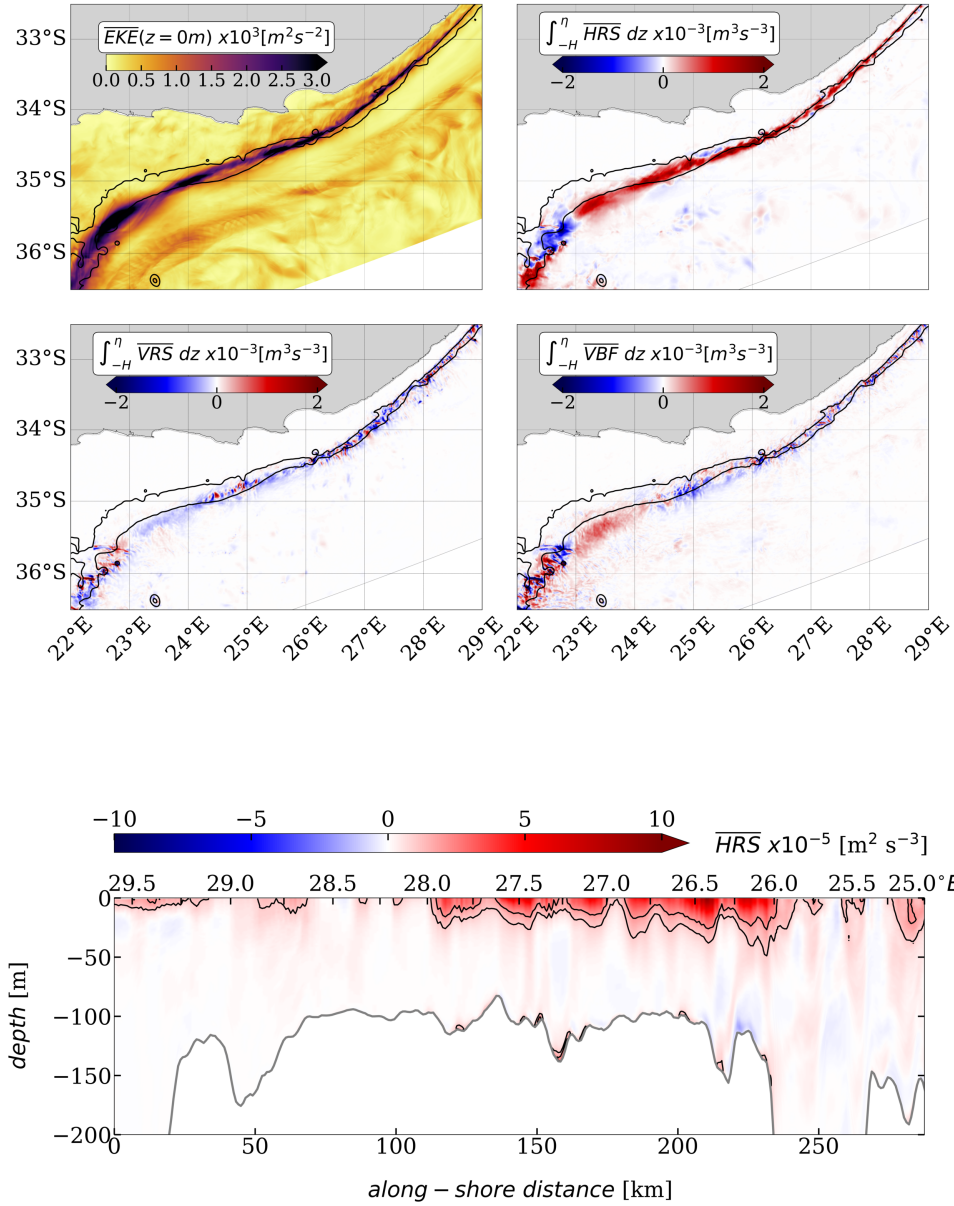


Figure 9. The cross-front velocity profile ($U(y)$ [m s^{-1}] in plain black line) and its fit (dashed black line) used as initial conditions in the 1D linear stability analysis are plotted (top). It is picked from the model at 5 m depth, at 28°E, just upstream of the submesoscale eddies generation, for a snapshot just before the submesoscale eddies develop. The relative vorticity gradient, $\frac{d^2U}{dy^2}$ [$\text{m}^{-1} \text{s}^{-1}$], computed for the initial velocity profile (plain grey line) and its fit (dashed grey line) are also plotted. This shows that the cross-front velocity profile satisfies the barotropic instability necessary condition. The perturbation growth rate [s^{-1}], resulting from the 1D linear stability analysis, is plotted as a function of wavelength [km] (bottom). This 1D linear stability analysis shows perturbations at the same scale (15 km) than the submesoscale eddies seen in the model (10-20 km) and in the SAGE dataset (15 km).



878
879
880
881
882
883
884
885
886
887

Figure 10. Top four panels : Maps of surface \overline{EKE} [$cm^2 s^{-2}$] and energy conversion rates \overline{HRS} , \overline{VRS} and \overline{VBF} [$m^{-3} s^{-3}$] integrated over the entire water column. The overbar denotes a week-long average. This average encompasses the Figure (4) snapshot (09/29 06:00) and corresponds to a full event of submesoscale eddies generation. Black contours represent the 200 m and 1000 m isobaths. When submesoscale eddies are presents, \overline{HRS} is the only term accounting for the energy transfer $MKE \rightarrow \overline{EKE}$. Bottom panel : Section along the vortex street, between 29.5 and 25 °E, of the energy conversion rate \overline{HRS} [$m^2 s^{-3}$]. The overbar denotes the same time average than in the top four panels. Black contours follow the 1 and 2 $m^2 s^{-3}$ \overline{HRS} isolines. The location of the section along the vortex street is shown as the white dashed line in Figure 7. The energy transfer $MKE \rightarrow \overline{EKE}$ occurs between the surface and 50 m deep.

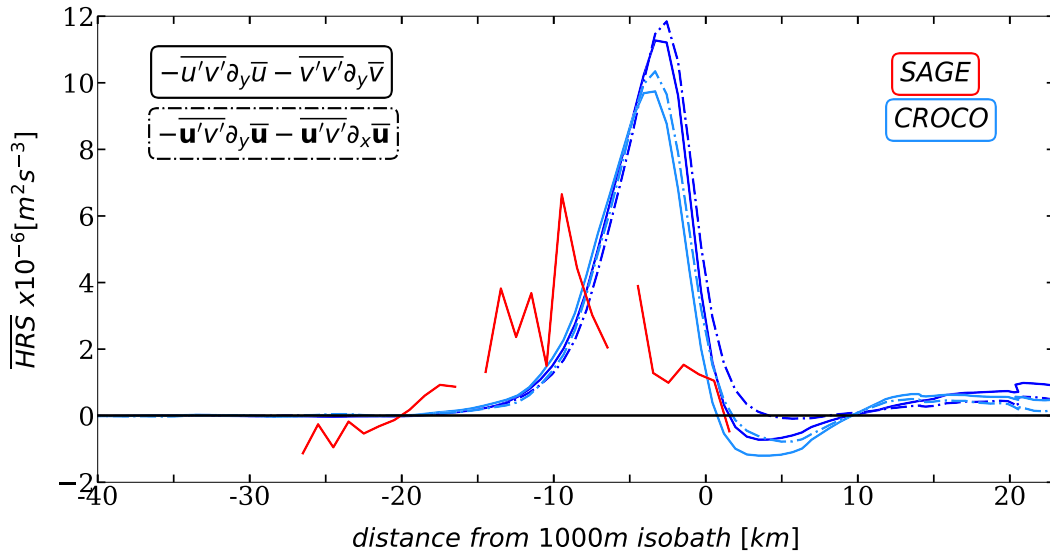


Figure 11. Cross-front sections at the SAGE location (25.75°E , shown in Figure 2a) for surface observed (red) and modeled (blue) partial and full \overline{HRS} rate. The partial \overline{HRS} rate, only composed of the cross-front derivatives subterms $(-\overline{u'v'}\partial_y\bar{u} - \overline{v'v'}\partial_y\bar{v})$, is shown for the SAGE dataset as a plain red line and for the model in plain blue lines. The full \overline{HRS} rate, composed of the cross and along-front derivatives subterms $(-\overline{u'u'}\partial_x\bar{u} - \overline{v'v'}\partial_y\bar{u})$ is shown in dashed blue lines. The modeled partial and full \overline{HRS} rates are computed for different time periods : a one-month long (light blue lines) and five consecutive-month without Natal Pulses (dark blue lines). The bottom x-axis represents the cross-front distance from the 1000 m isobath, which represents the front position for the SAGE period. The comparison between the modeled partial and full \overline{HRS} rates shows that the cross-front derivatives are a good *proxy* of the full \overline{HRS} rate. The comparison between the modeled 1 and 5 month averages of the \overline{HRS} rates shows that the submesoscale eddies generation is a locally recurrent process.

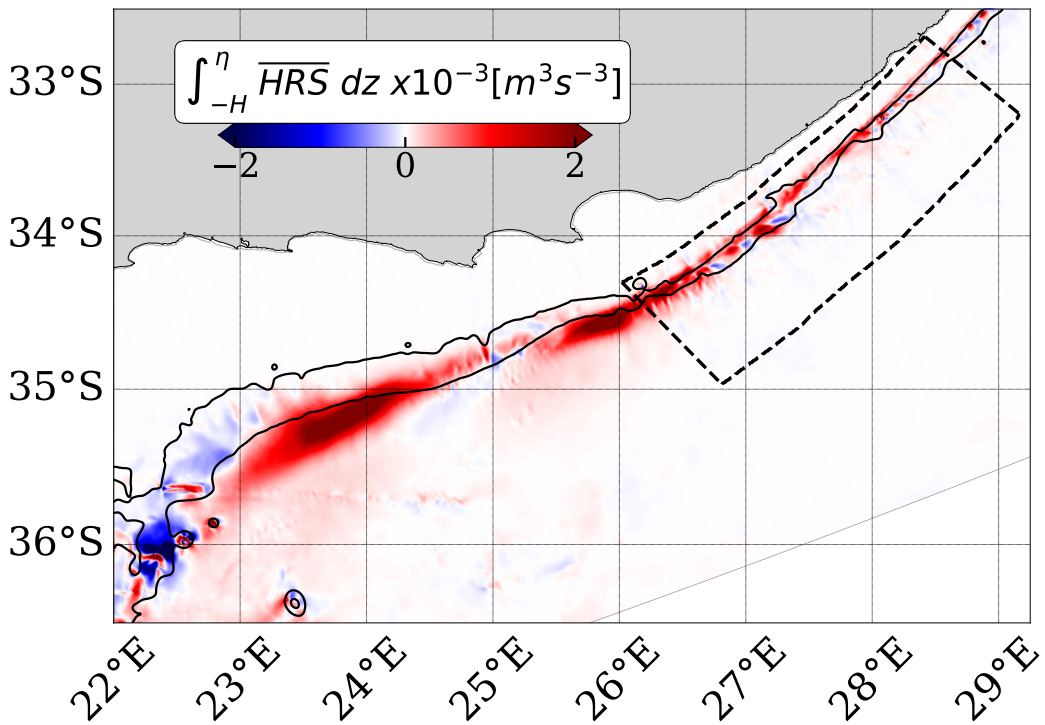


Figure 12. Map of energy conversion rate \overline{HRS} [m⁻³ s⁻³], integrated in the vertical. The overbar denotes a 5 month-long time average, when no Natal Pulse is present. Black contours are the 200 m and 1000 m isobaths. The black dashed box represents the area used for the computations of the along-front distributions (Figures 13) and of the time serie (Figure 15). The one-week (Figure 6) and 5 month-long time averages of \overline{HRS} show a similar pattern and confirm the hypothesis that submesoscale eddy generation is a locally recurrent process.

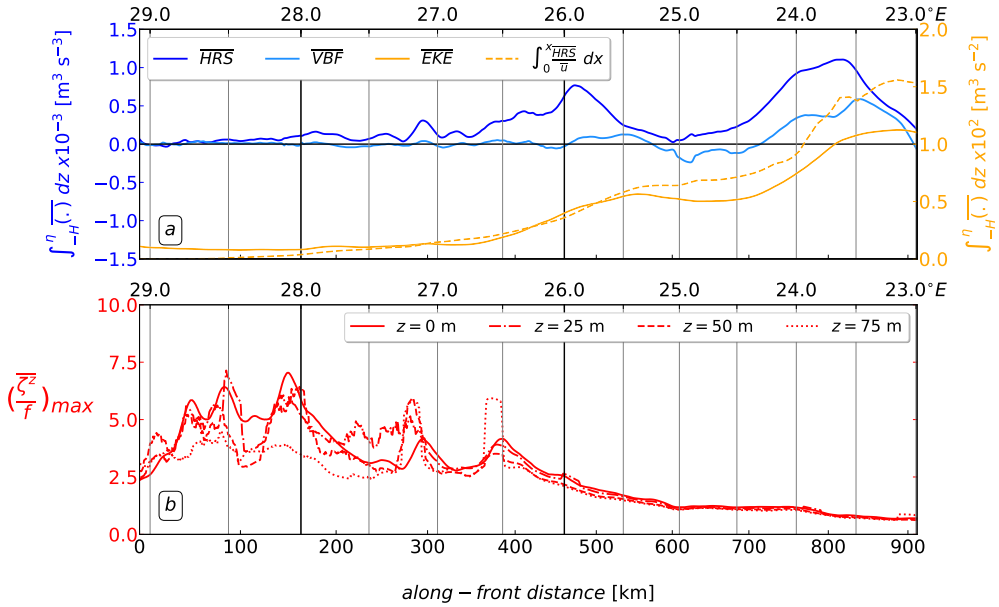
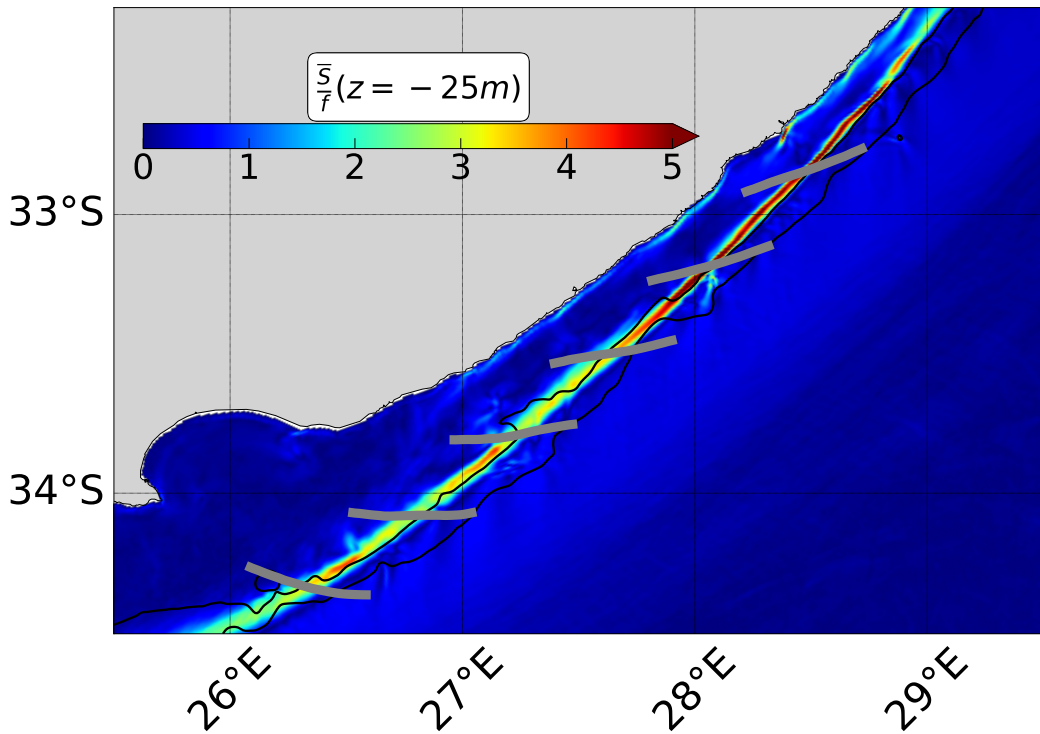
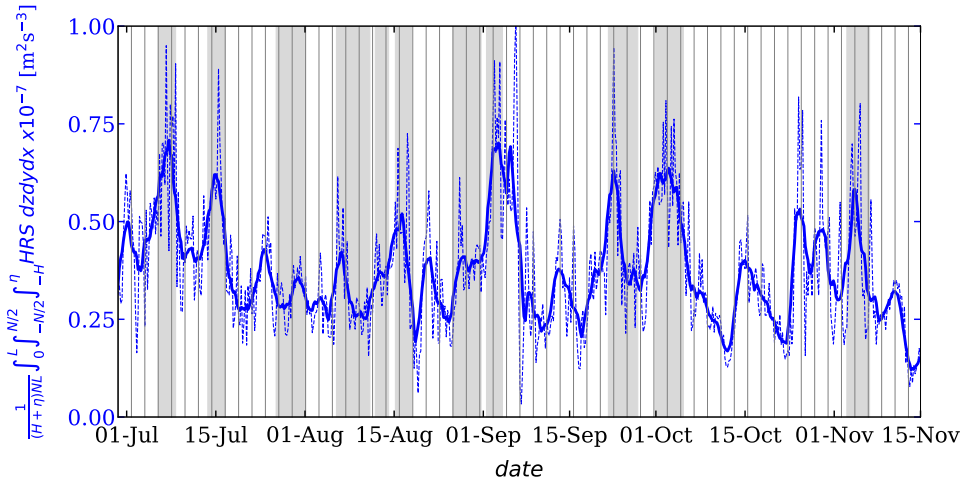


Figure 13. Along-front distributions of vertically integrated time mean energy conversion rate, \overline{HRS} [$\text{m}^3 \text{s}^{-3}$] of time mean EKE , \overline{EKE} [$\text{m}^3 \text{s}^{-2}$] and of $\int_0^x \frac{\overline{HRS}}{\bar{u}} dx$ [$\text{m}^3 \text{s}^{-2}$] (a). The along-front distributions result from a cross-front average over the width (of about 100 km) of the black dashed box centered on the inshore front shown in Figure 12. Cross-front maximum of mean relative vorticity, $\bar{\zeta}$, along the Agulhas front at the surface, 25, 50 and 75 m depth (b). In both panels, the reading direction for the along-front distributions corresponds to the current westward direction. The significant increase of \overline{HRS} and \overline{EKE} between 28°E and 26°E reflects the submesoscale eddies generation. Upstream of this front portion, the relative vorticity is large suggesting an unstable.

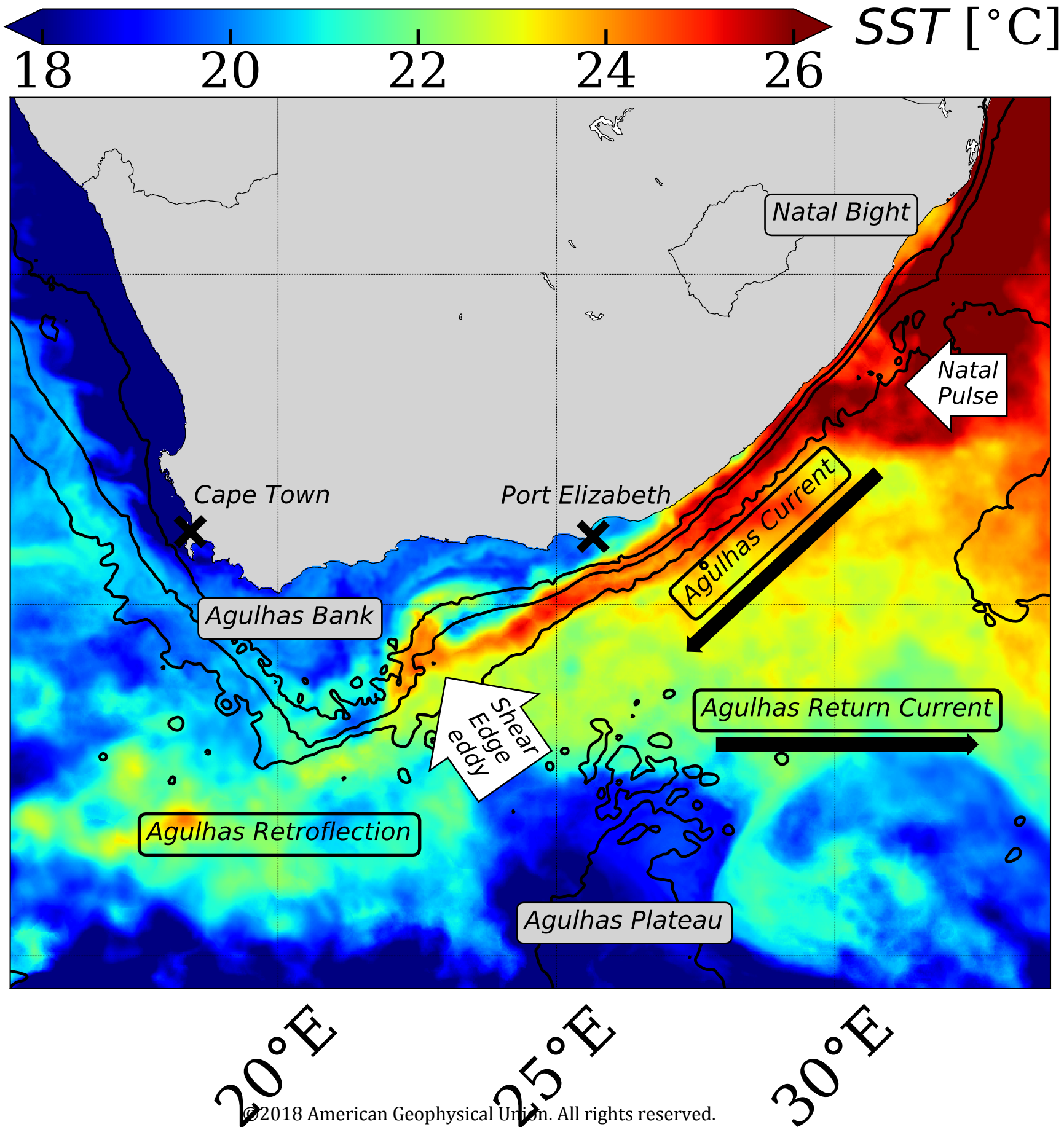


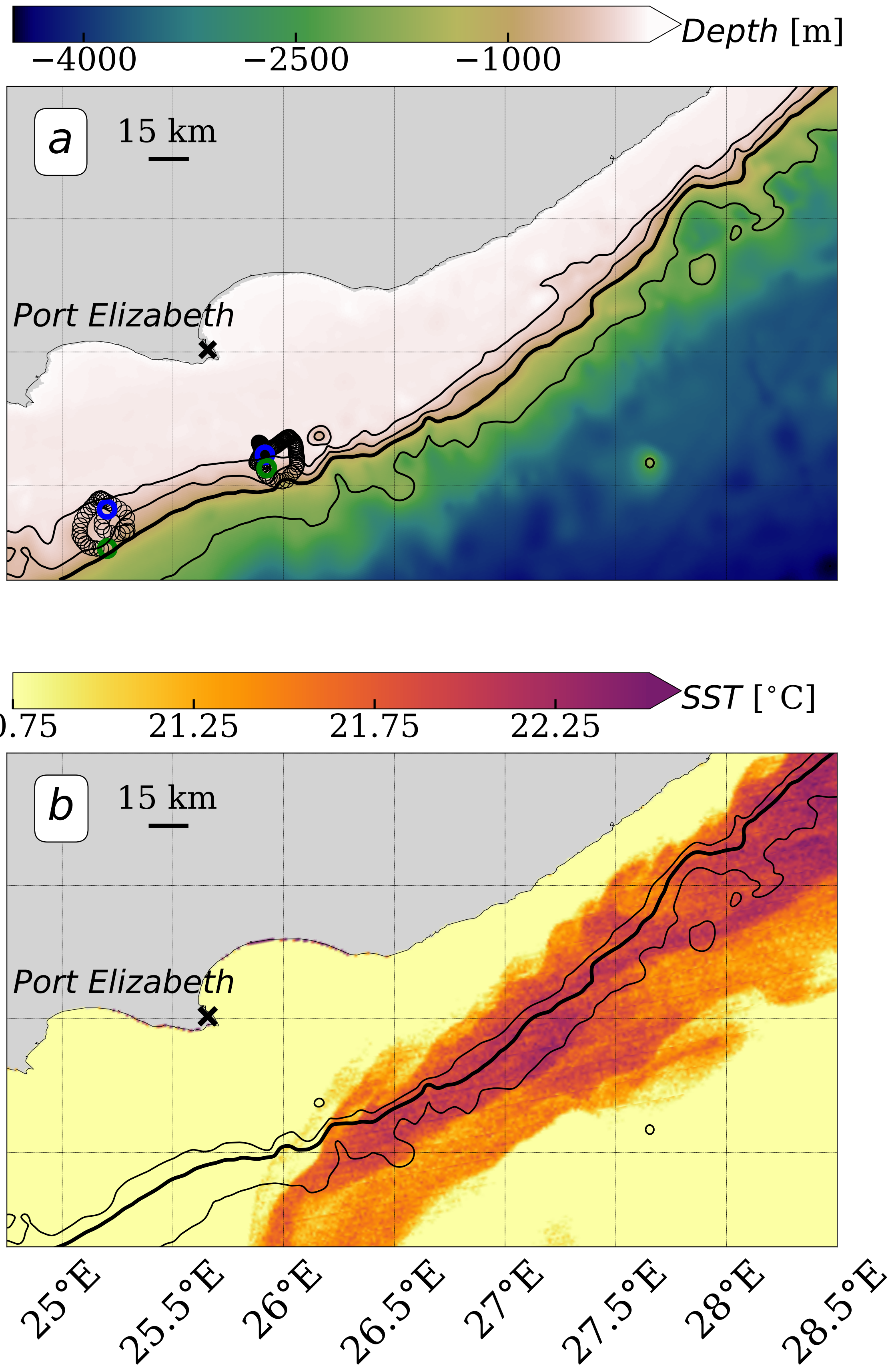
914 **Figure 14.** Map of the mean normalized background strain, $\overline{\frac{S}{f}}$ at 25 m. The overbar denotes
915 a 5 month time average, when no Natal Pulse is present. Grey segments represent the strain axis
16 and black contours the 200 m and 1000 m isobaths. High relative vorticity, found upstream of the
917 barotropic instability triggering (28°E), corresponds to where the background strain is the most
918 efficient at intensifying the front. The location of the barotropic instability triggering (between
919 28°E and 26°E , Figure 7) corresponds to where the background strain relaxes its constraint on the
0 front.



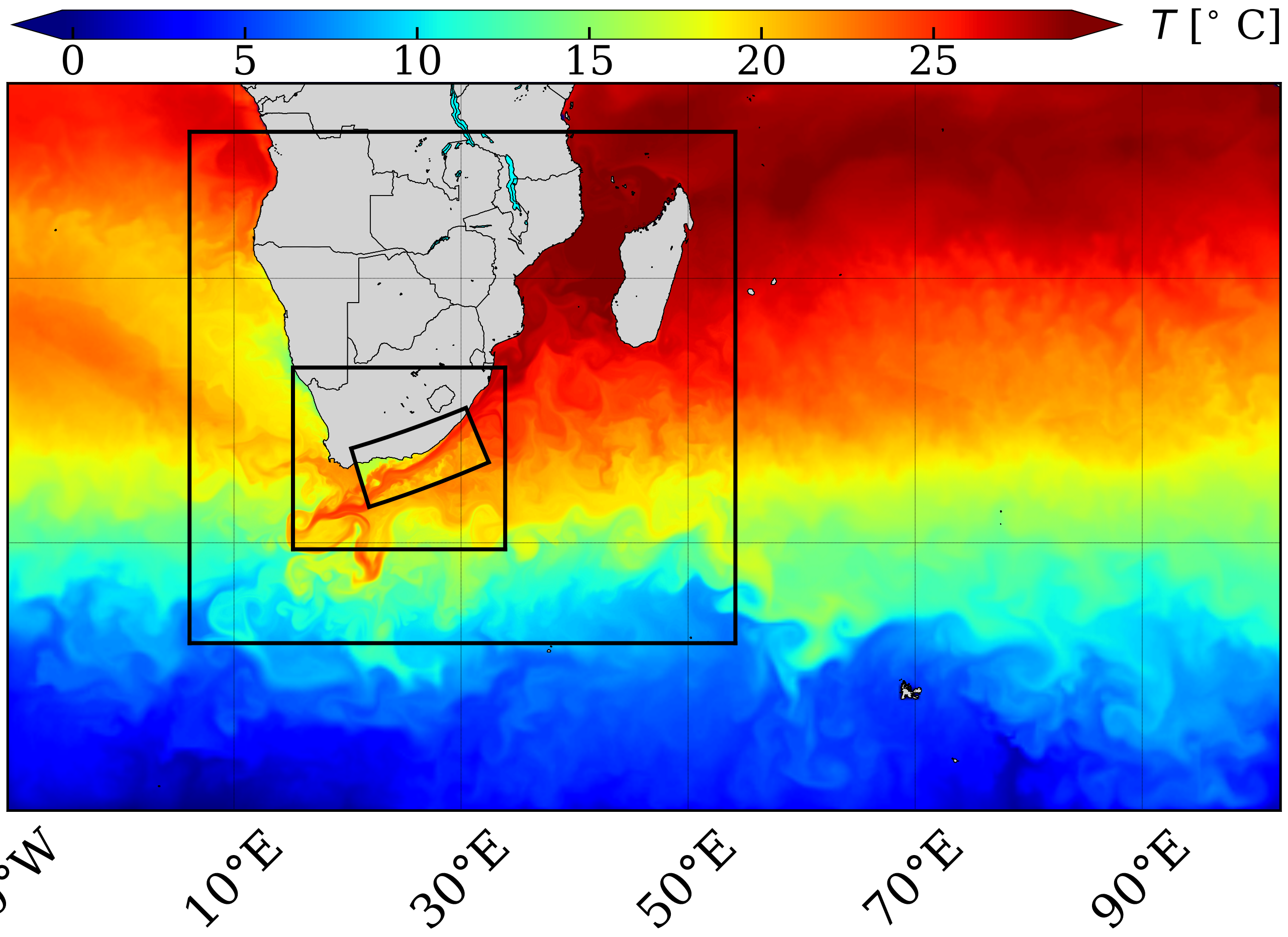
921 **Figure 15.** Time series of energy conversion rate HRS over a 5 month-long period when no
 922 Natal Pulse is present. The time series results from a volume average : on the vertical, HRS is
 923 averaged over the whole water column and on the horizontal over the 100 km wide black dashed
 924 box centered on the Agulhas front between 29°E and 26°E shown in Figure 12. The thin dashed
 925 and bold plain lines represent the raw and the smoothed (over a 10-point window) time series. The
 926 grey-shaded areas correspond to submesoscale eddies generation events identified from a movie a
 927 surface relative vorticity. Submesoscale eddies are generated when HRS is peaking, but the reverse
 928 is not true. This shows that a large HRS is not a sufficient condition to trigger instabilities and
 9 that submesoscale eddies generation result from a combination of several factors.

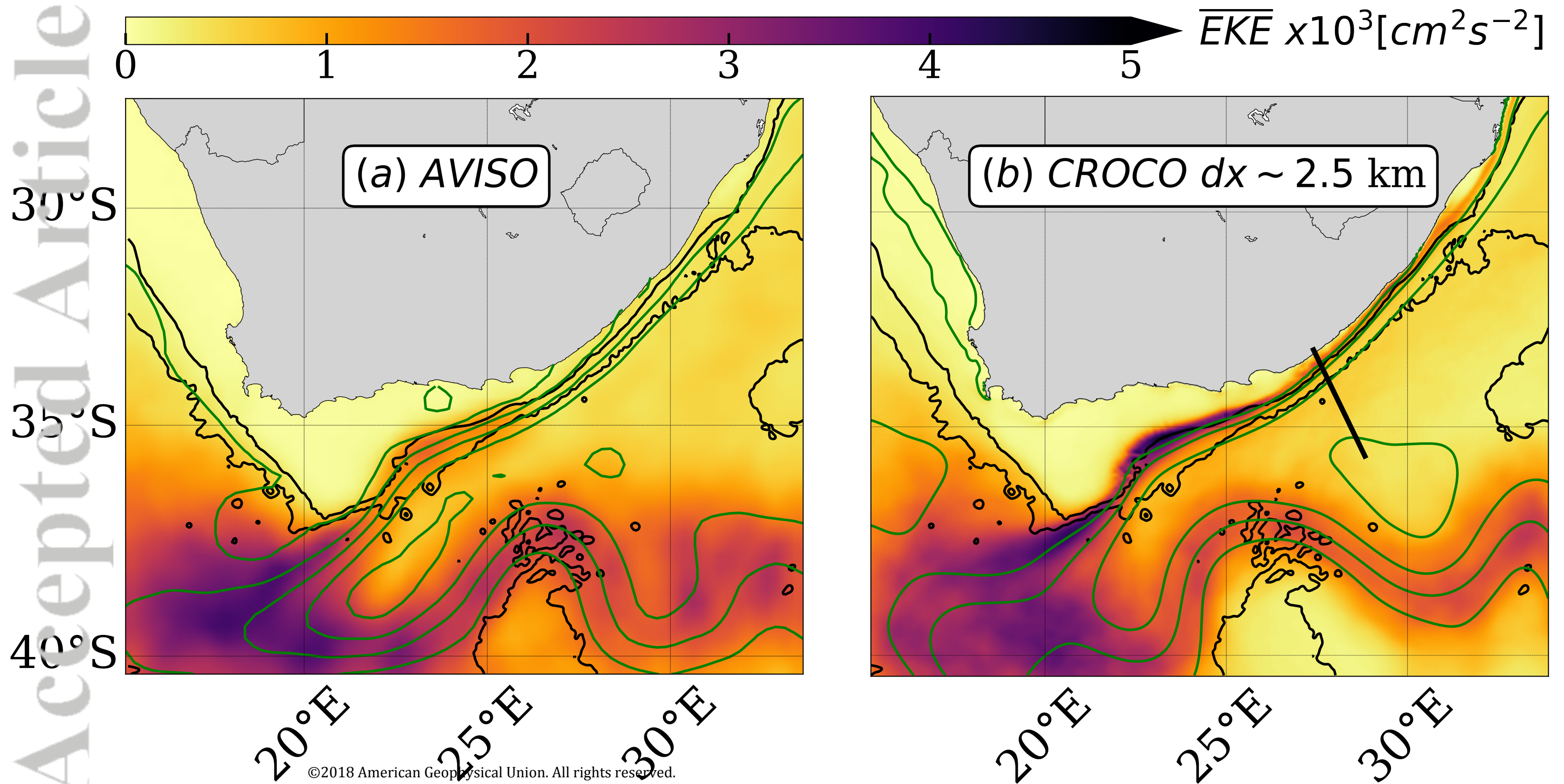
Accepted Article

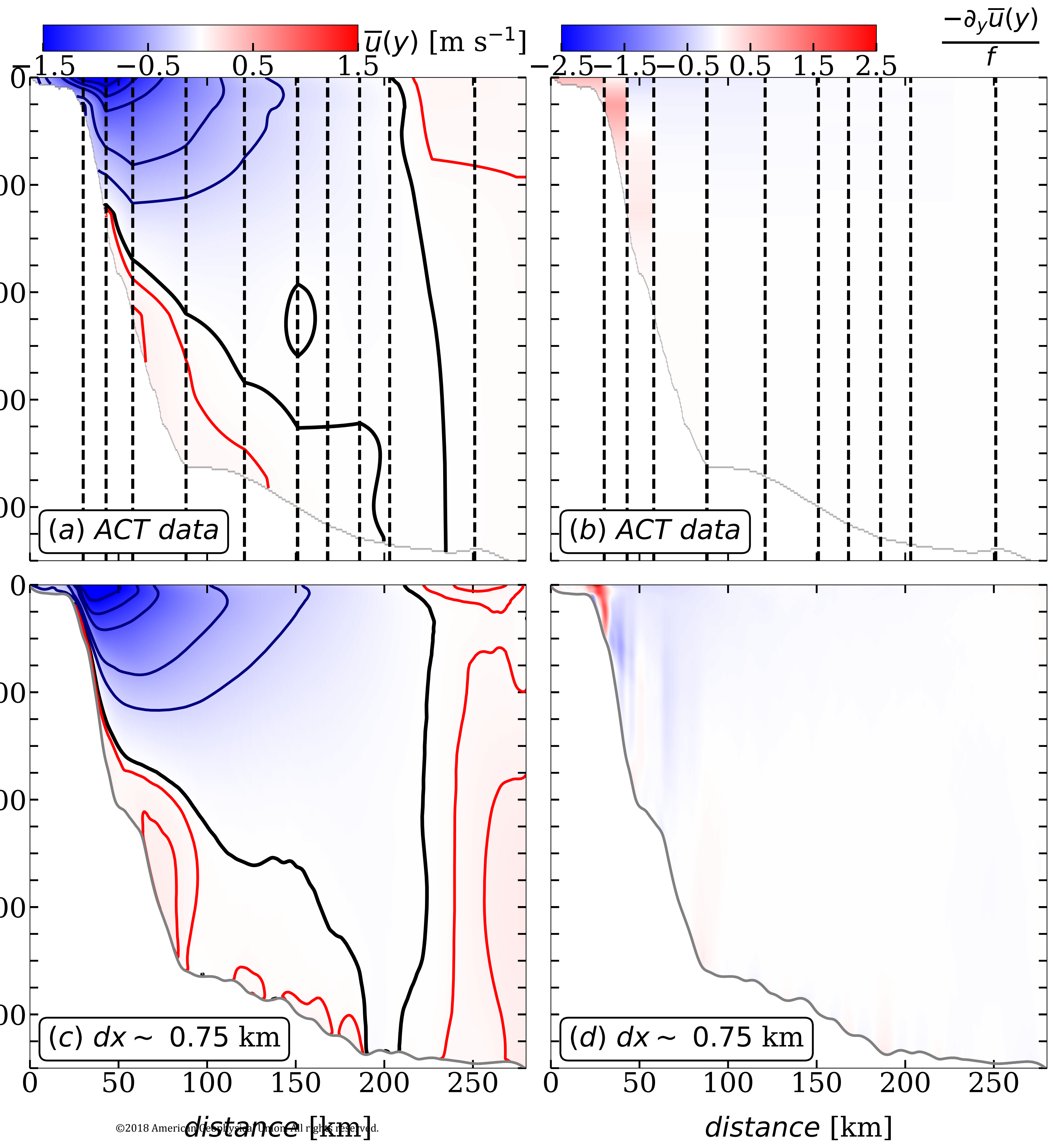


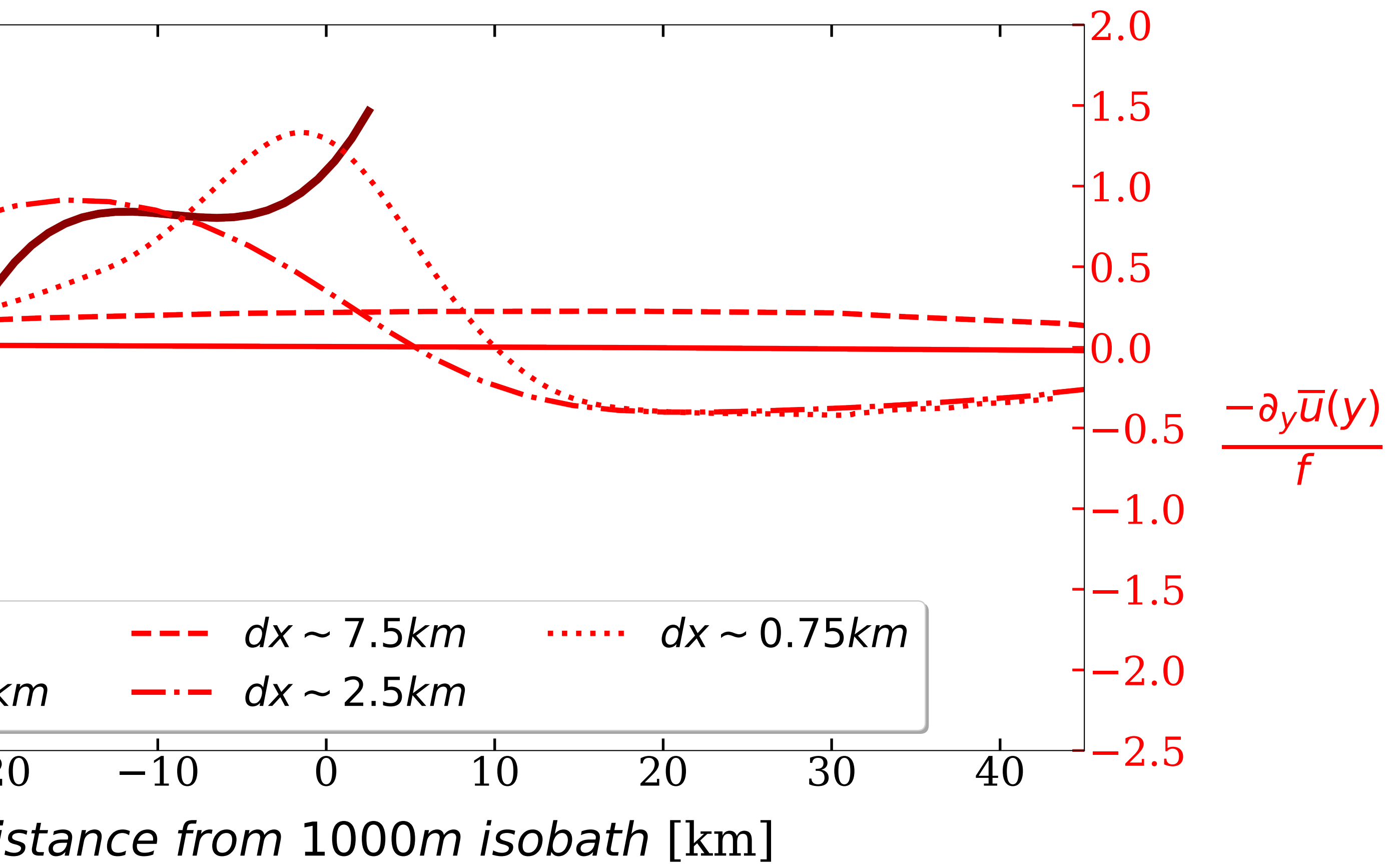
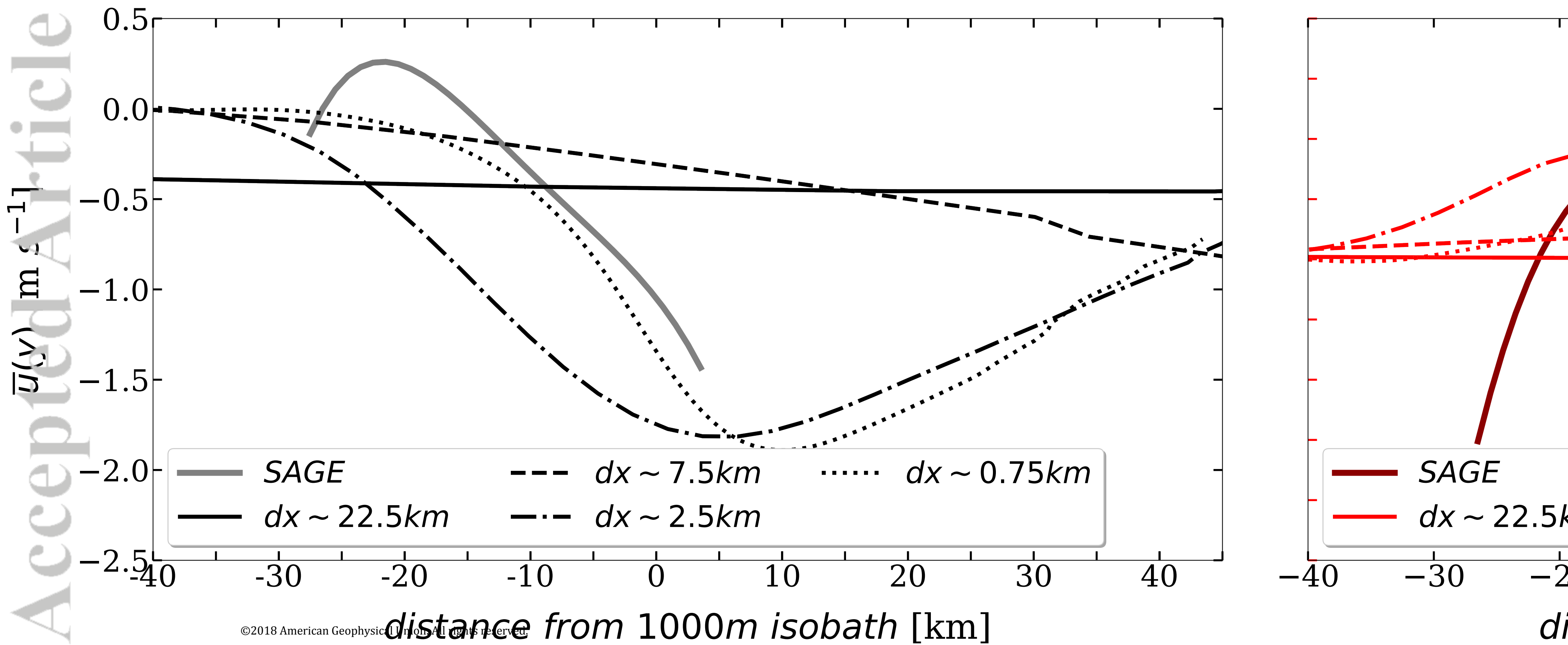


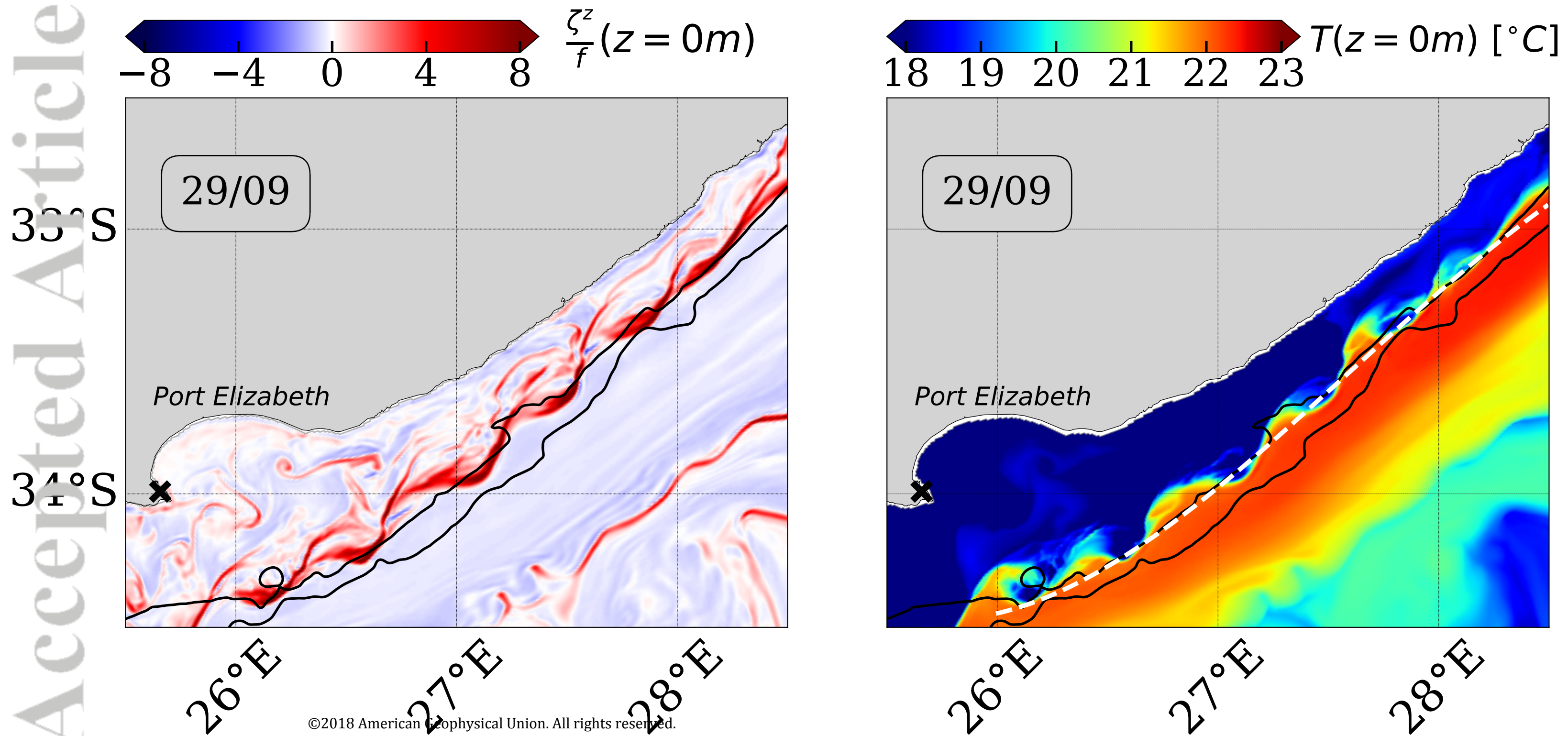
Accepted Article

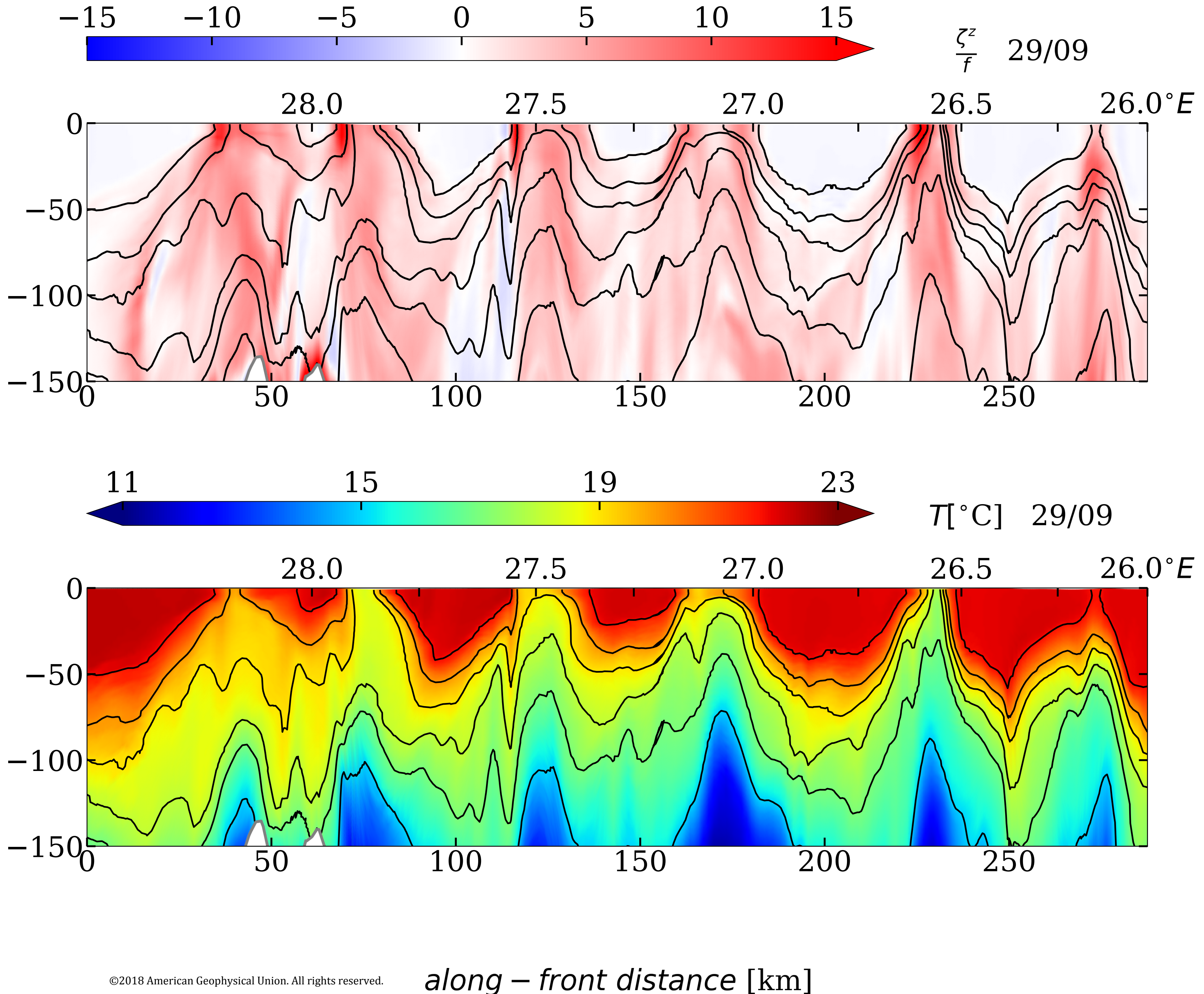


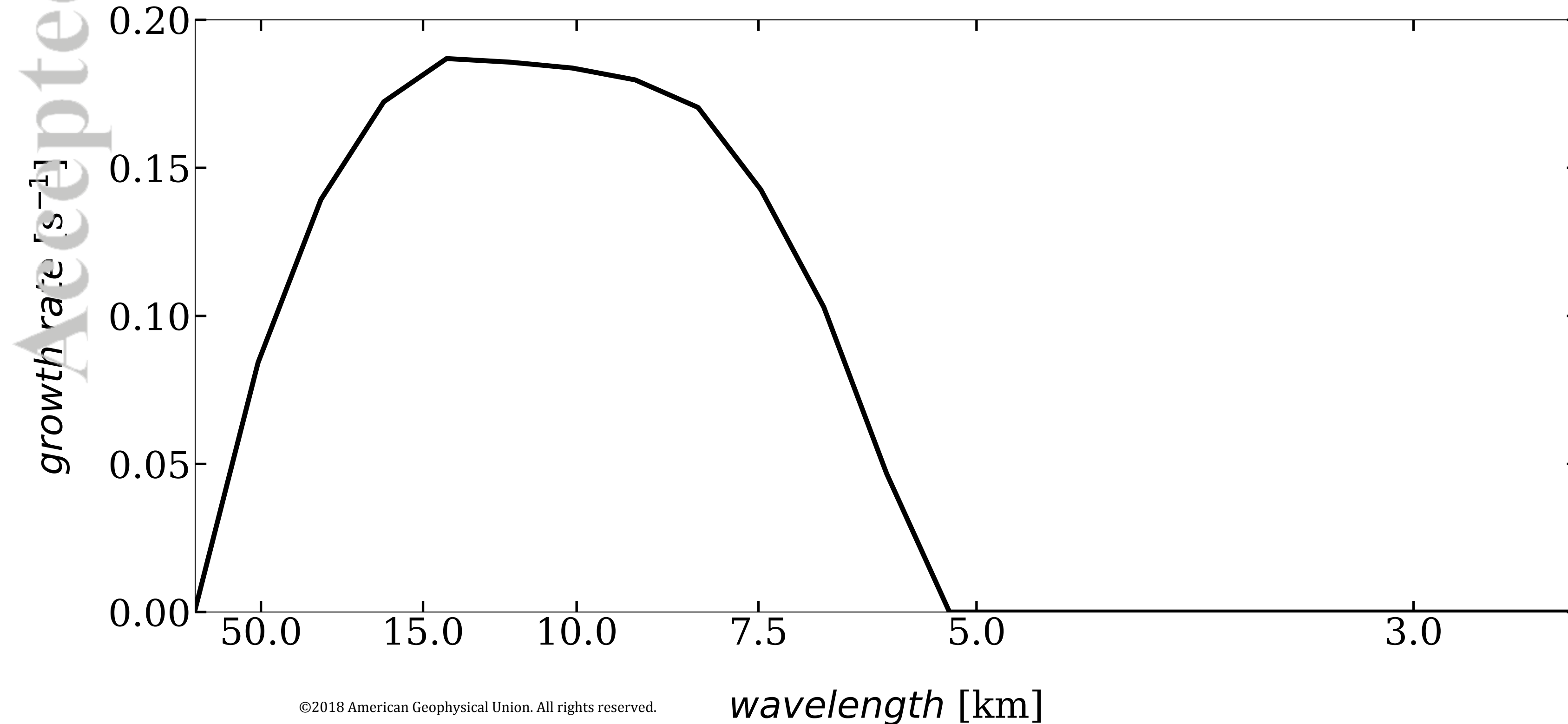
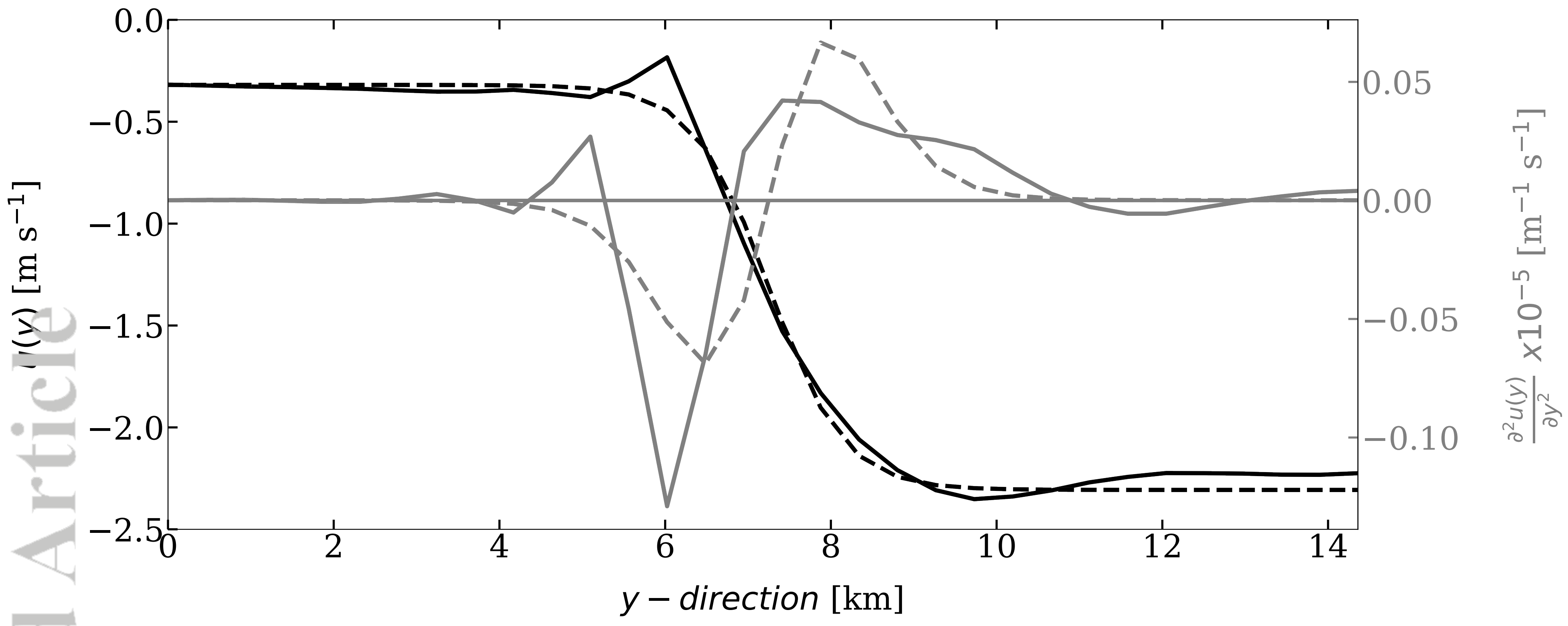


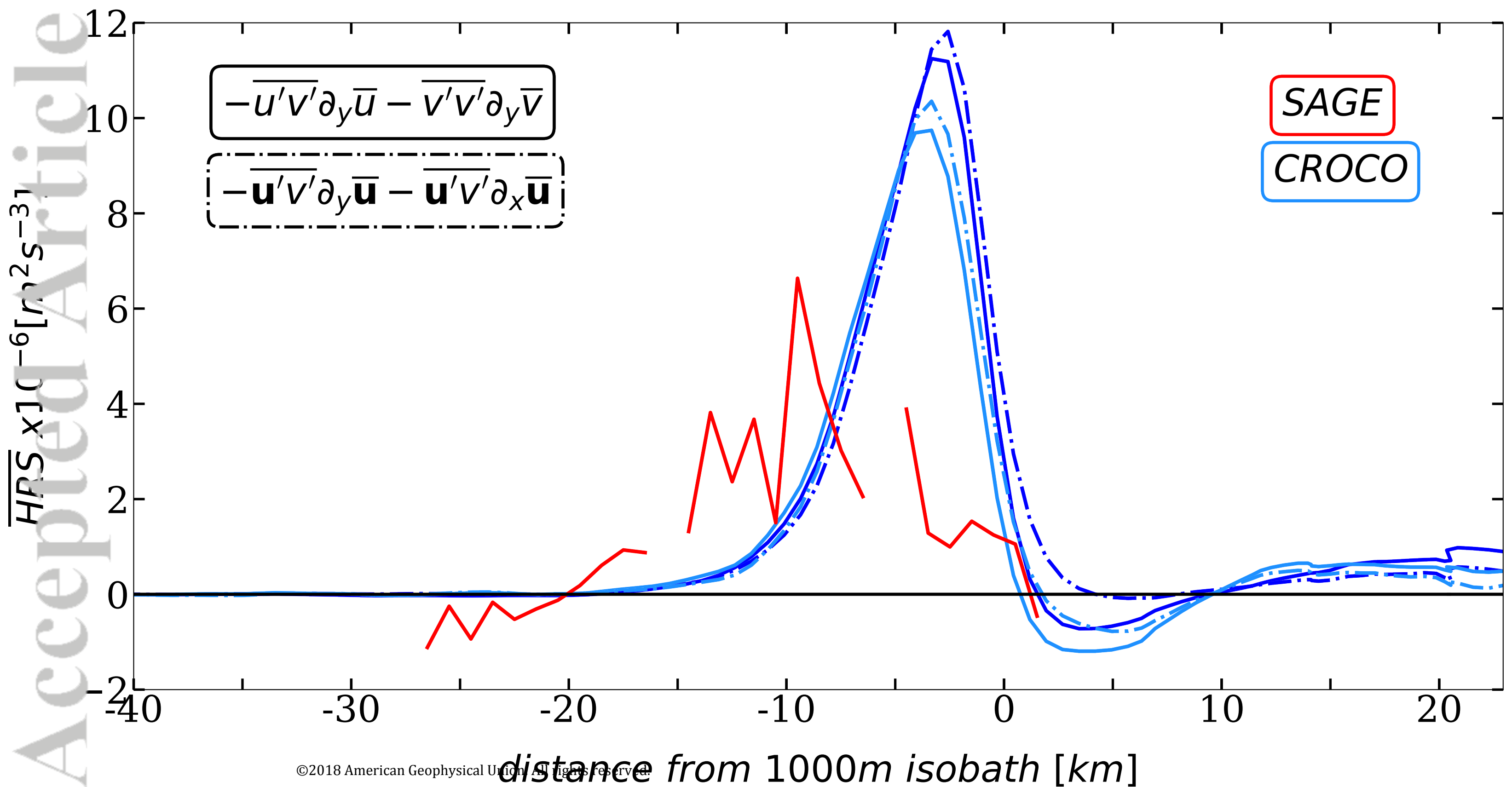




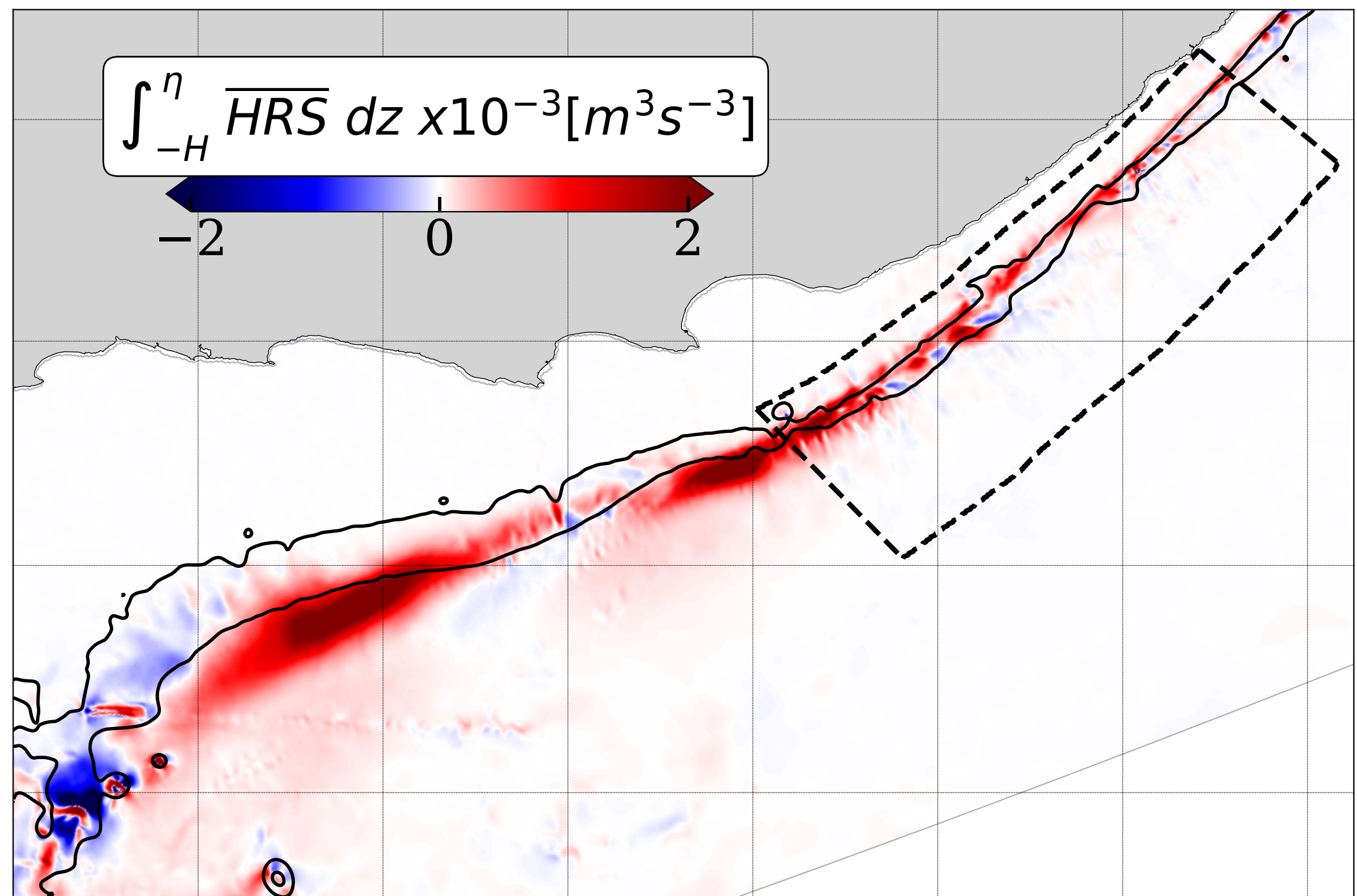








Accepted Article



Accepted Article

